

UNIVERSITY OF CALIFORNIA, SAN DIEGO

**Evidence of a new boson that decays to two W bosons in the full
leptonic final states in 24.4 fb^{-1} at center-of-mass energy of 7 and 8
TeV with Compact Muon Solenoid detector**

A dissertation submitted in partial satisfaction of the
requirements for the degree
Doctor of Philosophy

in

Physics

by

Jae Hyeok Yoo

Committee in charge:

Professor Frank Würthwein, Chair
Professor Claudio Campagnari
Professor Pamela Cosman
Professor Aneesh Manohar
Professor Avraham Yagil

2013

Copyright
Jae Hyeok Yoo, 2013
All rights reserved.

The dissertation of Jae Hyeok Yoo is approved, and it is acceptable in quality and form for publication on microfilm and electronically:

Chair

University of California, San Diego

2013

DEDICATION

To two, the loneliest number since the number one.

EPIGRAPH

*A careful quotation
conveys brilliance.*

—Smarty Pants

TABLE OF CONTENTS

Signature Page	iii
Dedication	iv
Epigraph	v
Table of Contents	vi
Acknowledgements	ix
Vita and Publications	x
Abstract of the Dissertation	xi
Chapter 1 Higgs Boson in Standard Model	1
1.1 Higgs Mechanism	2
1.1.1 How particles become massive : Higgs Mechanism	3
1.2 Production and Decay of Higgs Boson	9
1.2.1 Production of Higgs Boson	9
1.2.2 Decay of Higgs Boson	12
1.3 Limits on Higgs Boson Mass	15
1.3.1 Theoretical Limits	15
1.3.2 Experimental Limits	21
1.4 $H \rightarrow W^+W^- \rightarrow 2l2\nu$	23
1.4.1 Large expected signal yields	23
1.4.2 Angular distribution of leptons in the final state	24
1.4.3 Kinematic variables	25
1.4.4 CMS HWW results as of 2011	27
Chapter 2 LHC and CMS Detector	28
2.1 Large Hadron Collider	29
2.2 Compact Muon Solenoid detector	29
2.2.1 Tracker : pixel and silicon detector	29
2.2.2 ECAL	29
2.2.3 HCAL	29
2.2.4 Magnet	29
2.2.5 Muon System	29
2.2.6 Forward : HF	29
2.2.7 Computing : grid computing	29

Chapter 3	Event Reconstruction and Selection	30
3.1	Trigger	31
3.1.1	Analysis Triggers	31
3.1.2	Utility Triggers	33
3.2	Event Primary Vertex	34
3.3	Electron	35
3.4	Muon	36
3.5	Jet	37
3.6	Missing Transverse Energy	37
3.7	Top-tagging	37
Chapter 4	Efficiency Measurements	38
4.1	Lepton Efficiency	39
4.1.1	Electron Selection Efficiency	40
4.1.2	Muon Selection Efficiency	43
4.1.3	Trigger Efficiency	45
4.2	Jet Counting Efficiency	53
Chapter 5	Signal Extraction	56
5.1	Cut-based Method	57
5.2	Shape-based Method	57
Chapter 6	Background Estimation	58
6.1	WW	59
6.2	Top	59
6.3	DY	59
6.4	W+jets	59
6.5	Wgamma(*)	60
6.6	DYtt	60
6.7	WZ/ZZ	60
Chapter 7	Systematic Uncertainty	61
7.1	Instrumental Uncertainties	62
7.2	Background Estimation	62
7.3	Theoretical systematic uncertainties to signal	62
7.3.1	Jet Counting Efficiency	62
7.3.2	Acceptance	62
7.3.3	UEPS?	62
Chapter 8	Fit Validation	63
8.1	Validation of Fit Model	64
8.1.1	Fit Validation with Pseudo data	64
8.1.2	Fit Validation with Real data	64
8.1.3	Result on qqWW events : for qqWW	64

8.2	Post-fit Analysis	68
8.2.1	Post-fit result of nuisances	68
8.2.2	Correlations of nuisances	71
8.2.3	Post-fit normalization	74
Chapter 9	Statistical Interpretation	79
9.1	Exclusion of the Standard Model Higgs Boson	80
9.2	Discovery of a New Boson	83
9.3	Hypothesis Separation	84
Chapter 10	Study on Spin-Parity of the New Boson	85
Appendix A	Some Details on Statistical Procedure	86
A.1	Asimov data set	87
A.2	Asymtotic behavior of profiled LLR	87
Bibliography	88

ACKNOWLEDGEMENTS

Thanks to whoever deserves credit for Blacks Beach, Porters Pub, and every coffee shop in San Diego.

Thanks also to hottubs.

VITA

2007	B.S. in Physics, Korea University
2009	M.S. in Physics, Korea University
2013	Ph.D. in Physics, University of California, San Diego

PUBLICATIONS

Your Name, “A Simple Proof Of The Riemann Hypothesis”, *Annals of Math*, 314, 2007.

Your Name, Euclid, “There Are Lots Of Prime Numbers”, *Journal of Primes*, 1, 300 B.C.

ABSTRACT OF THE DISSERTATION

**Evidence of a new boson that decays to two W bosons in the full
leptonic final states in 24.4 fb^{-1} at center-of-mass energy of 7 and 8
TeV with Compact Muon Solenoid detector**

by

Jae Hyeok Yoo

Doctor of Philosophy in Physics

University of California, San Diego, 2013

Professor Frank Würthwein, Chair

This dissertation will be abstract.

Chapter 1

Higgs Boson in Standard Model

1.1 Higgs Mechanism

Properties of elementary particles in nature and their interactions (forces) to each other are described by Standard Model (SM) in particle physics. It is based on gauge symmetry and the group structure, $SU(3)_c \times SU(2)_L \times U(1)_Y$, where $SU(3)_c$, $SU(2)_L$, and $U(1)_Y$ describe color, weak isospin, and hyper charge, respectively. The gauge symmetry requires the weak gauge bosons to be massless, but we know that Weak gauge bosons, W^\pm and Z are massive. The cure for this is the Higgs mechanism which breaks $SU(2)_L \times U(1)_Y$ to $U(1)_{EM}$, thus giving mass to weak bosons but keeping photons massless.

1.1.1 How particles become massive : Higgs Mechanism

Since EW theory is based on $SU(2)$ symmetry, the Higgs field is given as a $SU(2)$ doublet,

$$\phi = \begin{pmatrix} \phi^+ \\ \phi^0 \end{pmatrix} \quad (1.1)$$

where each element is a complex field,

$$\phi^+ = \frac{\phi_1 + i\phi_2}{\sqrt{2}} \quad \text{and} \quad \phi^0 = \frac{\phi_3 + i\phi_4}{\sqrt{2}}. \quad (1.2)$$

We start with the Higgs Lagrangian to understand the essence of SSB before making the things more complicated. The full SM Lagrangian will be discussed after that. The Higgs Lagrangian is composed of kinetic and potential terms.

$$\mathcal{L}_\phi = \underbrace{(\partial_\mu \phi)^\dagger (\partial^\mu \phi)}_{\text{kinetic term}} - \underbrace{\left(\mu^2 \phi^\dagger \phi + \lambda (\phi^\dagger \phi)^2 \right)}_{\text{potential}} \quad (1.3)$$

where $\mu^2 < 0$ and $\lambda > 0$. The potential $V(\phi^\dagger \phi)$ is invariant under $SU(2)$ local gauge transformation,

$$\phi(x) \rightarrow \phi(x)' = e^{i\vec{\alpha}(x) \cdot \frac{\vec{\sigma}}{2}} \phi(x) \quad (1.4)$$

where $\vec{\alpha}(x)$ is a vector of parameters and $\vec{\sigma}$ is a vector of Pauli matrices. $V(\phi^\dagger \phi)$ has the minimum at $\phi^\dagger \phi = -\frac{\mu^2}{2\lambda} = \frac{v^2}{2}$ where v is the vacuum expectation value of the Higgs field ϕ . Due to the $SU(2)$ symmetry the choice of vacuum state is not definite as seen in the following equation,

$$\phi^\dagger \phi = \frac{1}{2} (\phi_1^2 + \phi_2^2 + \phi_3^2 + \phi_4^2) \quad (1.5)$$

This leads to an appropriate choice of vacuum for the physics of interest. We choose the vacuum state, ϕ_0

$$\phi_0 = \frac{1}{\sqrt{2}} \begin{pmatrix} 0 \\ v \end{pmatrix} \quad (1.6)$$

and expand around it by $H(x)$

$$\phi(x) = \frac{1}{\sqrt{2}} \begin{pmatrix} 0 \\ v + H(x) \end{pmatrix} \quad (1.7)$$

where $H(x)$ is the physical Higgs field. In order to make the lagrangian invariant under SU(2) transformation, the derivative ∂_μ should be replaced by the covariant derivative \mathcal{D}_μ

$$\mathcal{D}_\mu = \partial_\mu - ig_1 \frac{Y}{2} B_\mu - ig_2 \frac{\vec{\sigma}}{2} \cdot \vec{W}_\mu. \quad (1.8)$$

B_μ and \vec{W}_μ are the vector field(s) needed for U(1) and SU(2) gauge invariance, respectively. g_1 and g_2 are the couplings that decide the strength of interactions associated with B_μ and \vec{W}_μ . Y (weak hypercharge) and $\frac{\vec{\sigma}}{2}$ are the generators for U(1) and SU(2), respectively. Putting this into the Lagrangian \mathcal{L}_ϕ , the kinetic term becomes

$$(\mathcal{D}_\mu \phi)^\dagger (\mathcal{D}^\mu \phi) = \dots + \phi^\dagger \left[-ig_1 \frac{Y}{2} B^\mu - ig_2 \frac{\vec{\sigma}}{2} \cdot \vec{W}^\mu \right]^\dagger \left[-ig_1 \frac{Y}{2} B^\mu - ig_2 \frac{\vec{\sigma}}{2} \cdot \vec{W}^\mu \right] \phi$$

In order to derive masses of W and Z boson, we use the vacuum state of Higgs field ϕ_0 because mass are present even without dynamical field. With $Y = 1$ and $\phi = \frac{1}{\sqrt{2}} \begin{pmatrix} 0 \\ v \end{pmatrix}$, writing the explicitly in 2×2 matrices,

$$\begin{aligned} & \frac{1}{8} \left| \begin{pmatrix} g_1 B_\mu + g_2 W_\mu^3 & g_2(W_\mu^1 - iW_\mu^2) \\ g_2(W_\mu^1 + iW_\mu^2) & g_1 B_\mu - g_2 W_\mu^3 \end{pmatrix} \begin{pmatrix} 0 \\ v \end{pmatrix} \right|^2 \\ &= \frac{v^2}{8} \left| \begin{pmatrix} g_2(W_\mu^1 - iW_\mu^2) \\ g_1 B_\mu - g_2 W_\mu^3 \end{pmatrix} \right|^2 \\ &= \frac{v^2 g_2^2}{8} \left[(W_\mu^1)^2 + (W_\mu^2)^2 \right] + \frac{v^2}{8} (g_1 B_\mu - g_2 W_\mu^3)^2 \end{aligned} \quad (1.10)$$

The first term can be written converting W^1 and W^2 into charge states $W^\pm = \frac{1}{\sqrt{2}} (W^1 \mp iW^2)$,

$$\frac{1}{2} \left(\frac{vg_2}{2} \right)^2 \left[(W_\mu^+)^2 + (W_\mu^-)^2 \right]. \quad (1.11)$$

Thus, we have the mass of charged W boson $M_W = \frac{vg_2}{2}$. Now we know that the second term in 1.10 should correspond Z boson because that is the only remaining mass boson. Because the mixed fields should have the same normalization, the

physical field for Z boson Z_μ is

$$Z_\mu = \frac{(g_1 B_\mu - g_2 W_\mu^3)}{\sqrt{g_1^2 + g_2^2}} \quad (1.12)$$

which gives its mass $M_Z = \frac{v}{2}\sqrt{g_1^2 + g_2^2}$. We have an orthogonal field that is massless (thus mass term does not appear in the Lagrangian),

$$A_\mu = \frac{(g_1 B_\mu + g_2 W_\mu^3)}{\sqrt{g_1^2 + g_2^2}} \quad (1.13)$$

This is the field that remains unbroken by SSB. So, it corresponds to photon. Rewriting the Lagrangian using the physical weak boson states W_μ^\pm and Z_μ , and their masses, we have the following terms for interactions between Higgs and weak bosons,

$$2\frac{M_W^2}{v}H(x)(W_\mu^+)^2 + \frac{M_Z^2}{v}H(x)(Z_\mu)^2 + \frac{M_W^2}{v^2}H(x)^2(W_\mu^+)^2 + \frac{M_Z^2}{2v^2}H(x)^2(Z_\mu)^2 \quad (1.14)$$

For Higgs-Weak boson interactions, the couplings are proportional to the square of weak boson mass. The corresponding Feynman diagrams are shown in Fig 1.1.

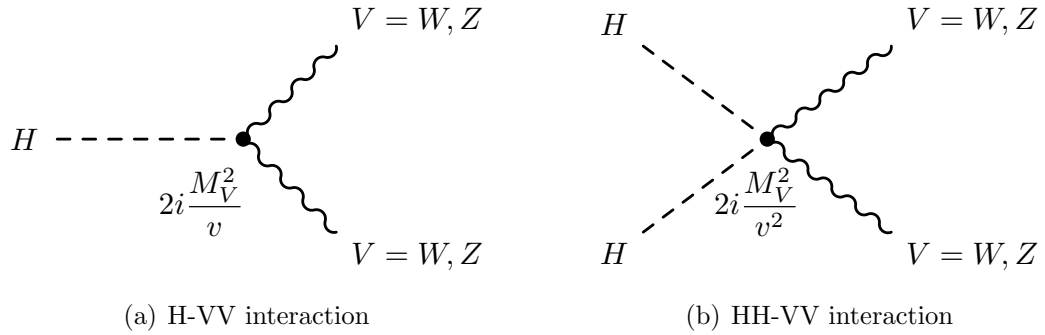


Figure 1.1: Feynman diagrams for (a) H-VV and (b) HH-VV interactions.

Considering additional factorials due to identical particles, the vertex factors can be written as $2i\frac{M_V^2}{v}$ and $2i\frac{M_V^2}{v^2}$ for HVV and HHV, respectively, where V denotes W or Z. After SSB, the Higgs potential term, $\mu^2\phi^\dagger\phi + \lambda(\phi^\dagger\phi)^2$, in the Lagrangian

becomes

$$\mathcal{L}_{\text{Higgs Potential}} = \mu^2 \phi^\dagger \phi + \lambda (\phi^\dagger \phi)^2 \quad (1.15)$$

$$= \frac{\mu^2}{2}(v + H)^2 + \frac{\lambda}{4}(v + H)^4 \quad (1.16)$$

$$= \dots - \mu^2 H^2 - \frac{\mu^2}{v} H^3 - \frac{\mu^2}{4v^2} H^4 \quad (1.17)$$

where H^0 and H^1 terms are ignored in the last line. **I remember that the first order term does not affect the lagrangian, but do not remember the argument.** From the above eq., the Higgs mass is identified as $m_H^2 = -2\mu^2$. Rewriting the eq, using this definition, we have

$$\mathcal{L}_{\text{Higgs Potential}} = \dots - \frac{1}{2}m_H^2 H^2 - \frac{m_H^2}{2v} H^3 - \frac{m_H^2}{8v^2} H^4 \quad (1.18)$$

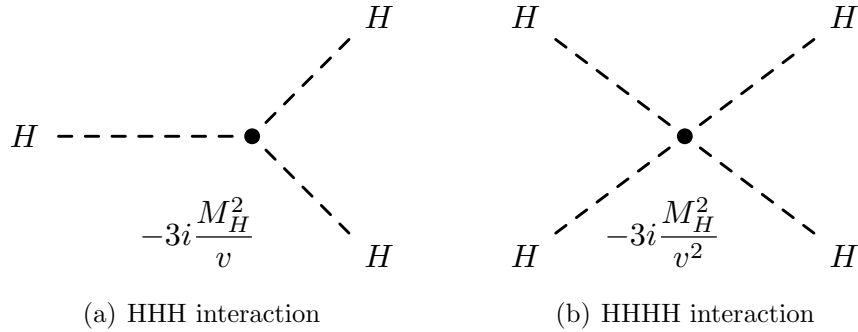


Figure 1.2: Feynman diagrams for (a) HHH and (b) HHHH interactions.

The corresponding Feynman diagrams are shown in Fig 1.2. Now we see that the entire Higgs sector depends on m_H and v . The v is calculated by $v = (\sqrt{2}G_F)^{-1/2} = 246 \text{ GeV}$ where G_F is the Fermi constant which is extracted from measurement of muon lifetime. Thus, the SM Higgs sector is fully described by m_H . m_H is a function of λ and v , $m_H^2 = 2\lambda v^2$ and we do not know the physical meaning of λ , the mass of Higgs boson is not predictable by theory. It's experimentalist's task to measure m_H and complete the Standard Model of particle physics.

The introduced Higgs field had 4 degrees of freedom, ϕ_1, ϕ_2, ϕ_3 and ϕ_4 . But, we chose the Higgs field to have only one degree of freedom, $H(x)$. Where did the three go? By breaking $SU(2)_L \times U(1)_Y$ to $U(1)_{EM}$, the three gauge bosons

acquired masses. This was done by adding longitudinal components to the three bosons. Thus, now we have one physical Higgs field and three massive and one massless gauge bosons instead of four unphysical Higgs fields and four massless gauge bosons.

The fermions acquire mass by interaction with Higgs field. Let's start with leptons whose case is simpler than quarks due to absence of right-handed neutrinos, *i.e.* neutrinos are massless. Below, e means leptons. We can add $SU(2)$ -invariant terms to the Lagrangian. Table 1.1.1 shows the quantum numbers for $SU(2) \times U(1)$.

	T_3	Y
$\begin{pmatrix} \nu_L \\ e_L \end{pmatrix}$	$\frac{1}{2}$	-1
ν_R	0	0
e_R	0	-2
$\begin{pmatrix} \phi_+ \\ \phi_0 \end{pmatrix}$	$\frac{1}{2}$	-1

Table 1.1: $SU(2) \times U(1)$ quantum numbers

From the table, one can see that the interaction such as

$$e_R + \begin{pmatrix} \phi_+ \\ \phi_0 \end{pmatrix} \rightarrow \begin{pmatrix} \nu_L \\ e_L \end{pmatrix} \quad (1.19)$$

conserves quantum numbers. Given the structure of the interaction, we specify the strength with g_e . Including the hermitian conjugate to the Lagrangian, the lepton-Higgs interaction term becomes

$$\mathcal{L}_{int,lepton} = -g_e \left[\begin{pmatrix} \bar{\nu}_L & \bar{e}_L \end{pmatrix} \begin{pmatrix} \phi_+ \\ \phi_0 \end{pmatrix} e_R + \bar{e}_R \begin{pmatrix} \bar{\phi}_+ & \bar{\phi}_0 \end{pmatrix} \begin{pmatrix} \nu_L \\ e_L \end{pmatrix} \right] \quad (1.20)$$

Using the Higgs field used in SSB $\frac{1}{\sqrt{2}} \begin{pmatrix} 0 \\ v + H(x) \end{pmatrix}$, the Lagrangian is calculated to be

$$\mathcal{L}_{int,lepton} = -\frac{g_e v}{\sqrt{2}} (\bar{e}_L e_R + \bar{e}_R e_L) - \frac{g_e H}{\sqrt{2}} (\bar{e}_L e_R + \bar{e}_R e_L) \quad (1.21)$$

Since $\bar{e}e = \bar{e}(P_L^2 + P_R^2)e = \bar{e}_L e_R + \bar{e}_R e_L$ where P_L and P_R are projection operators, the first term $-\frac{g_e v}{\sqrt{2}} \bar{e}e$ corresponds to the mass term for lepton. Thus, the mass is identified to be

$$m_e = \frac{g_e v}{\sqrt{2}}. \quad (1.22)$$

Rewriting the Lagrangian in terms of m_e instead of an arbitrary g_e , we get

$$\mathcal{L}_{int} = -m_e \bar{e}e - \frac{m_e}{v} \bar{e}e H. \quad (1.23)$$

Since there isn't a physical motivation for g_e , m_e is not calculable by theory, but needs to be experimentally determined. The second term corresponds to lepton-Higgs interaction. The size of the interaction is proportional to the mass of lepton. Thus, light quarks have very weak couplings to Higgs fields. For example, electron has $\frac{m_e}{v} = \frac{0.5 \text{ MeV}}{246 \text{ GeV}} \sim \mathcal{O}(10^{-6})$ and muon has $\frac{106 \text{ MeV}}{246 \text{ GeV}} \sim \mathcal{O}(10^{-3})$.

The case for quarks is more complicated due to presence of right-handed up-type quarks opposite to lepton case. In order to generate masses for up-type quarks, we need a new Higgs doublet

$$\phi_c = i\sigma_2 \phi^* = \begin{pmatrix} \phi_0^* \\ -\phi_- \end{pmatrix} = \frac{1}{\sqrt{2}} \begin{pmatrix} v + H(x) \\ 0 \end{pmatrix}. \quad (1.24)$$

The new Higgs field is invariant under $SU(2)$ transformation and has $Y = -1$.

$$\mathcal{L}_{int,quark} = -g_d \left[\begin{pmatrix} \bar{u}_L & \bar{d}_L \end{pmatrix} \begin{pmatrix} \phi_+ \\ \phi_0 \end{pmatrix} d_R \right] - g_u \left[\begin{pmatrix} \bar{u}_L & \bar{d}_L \end{pmatrix} \begin{pmatrix} \phi_0^* \\ -\phi_+ \end{pmatrix} u_R \right] \quad (1.25)$$

$$= -\frac{g_d v}{\sqrt{2}} \bar{d}d - \frac{g_d H}{\sqrt{2}} \bar{d}d - \frac{g_u v}{\sqrt{2}} \bar{u}u - \frac{g_u H}{\sqrt{2}} \bar{u}u \quad (1.26)$$

$$= -m_d \bar{d}d - \frac{m_d}{v} \bar{d}d H - m_u \bar{u}u - \frac{m_u}{v} \bar{u}u H \quad (1.27)$$

where

$$m_d = \frac{g_d v}{\sqrt{2}} \quad \text{and} \quad m_u = \frac{g_u v}{\sqrt{2}} \quad (1.28)$$

is used as the lepton case. The strength of interaction depends on the fermion mass, m_f/v .

Fig. 1.3 shows Feynman diagram for Higgs - fermion interaction.

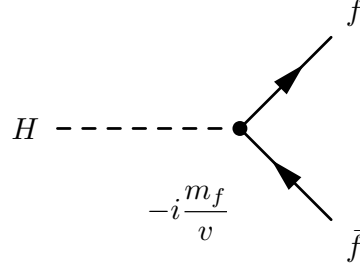


Figure 1.3: Feynman diagram for Hff interaction.

1.2 Production and Decay of Higgs Boson

1.2.1 Production of Higgs Boson

Standard model Higgs boson is generated by 4 major processes, gluon-gluon fusion (ggH : $gg \rightarrow H$), vector boson fusion (qqH : $q\bar{q} \rightarrow H$), associated production with vector bosons (VH : $q\bar{q} \rightarrow VH$), and associated production with heavy quarks (QQH : $q\bar{q} \rightarrow Q\bar{Q}H$). Figure X.X shows the Feynman diagrams corresponding those mechanisms. Since H does not couple to gluon in ggH process it is produced via a top loop. At LHC ggH has the largest production rate due to PDF and the heaviness of top quark.

At hadron collider the hadronic cross section(σ) is calculated with parton-level cross-section ($\hat{\sigma}$) convoluted with PDF,

$$\sigma(pp \rightarrow H + X) = \sum_{i,j} \int dx_1 dx_2 f_i(x_1) f_j(x_2) \hat{\sigma}(ij \rightarrow H + X) \quad (1.29)$$

where i and j are colliding partons, x_1 and x_2 are longitudinal momentum fractions carried by i and j. Each component in the equation is subject to the following uncertainties. The partonic cross section is calculated at given a renormalization scale μ_R and a factorization scale μ_F . Due to possible uncalculated higher-order QCD radiative corrections, the uncertainty is estimated by varying the scales around the central values. In the de Florian and Grazzini (dFG) calculation [ref], the central values are chosen to be $\mu_0 = m_H$. The scales μ_R and μ_F are varied are in the range $\frac{1}{2}\mu_0 < \mu_F, \mu_R < 2\mu_0$ with a constraint $\frac{1}{2} < \frac{\mu_F}{\mu_R} < 2$. PDF is obtained by fitting on data measured in deep-inelastic scattering, Drell-Yan, and jet production from

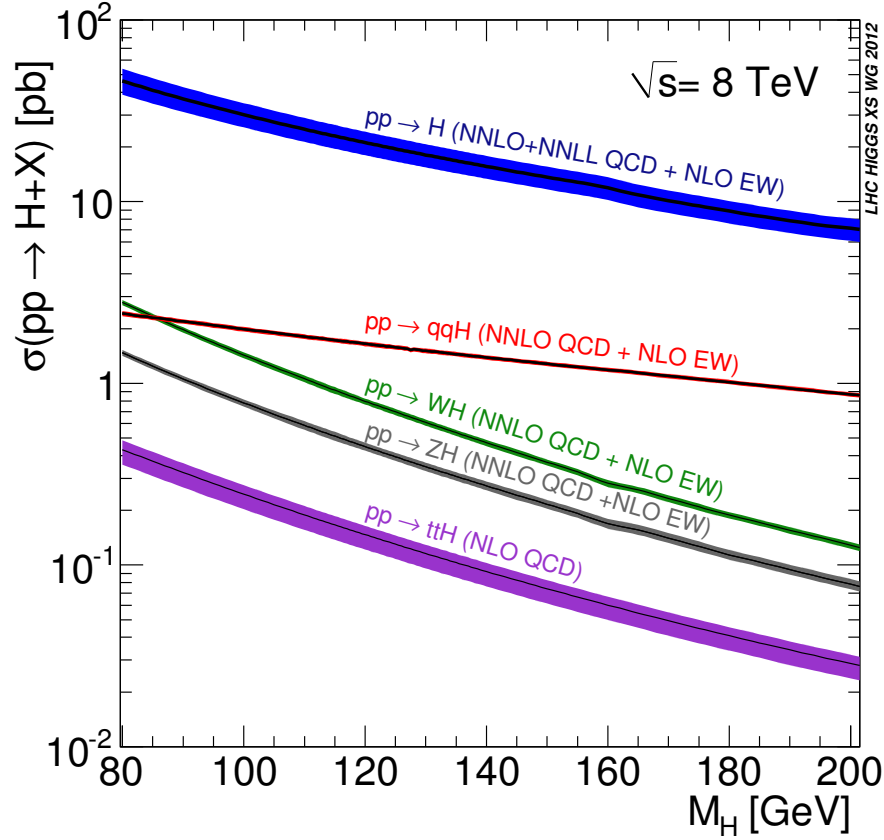


Figure 1.4: Standard model Higgs production cross sections as a function of m_H at $\sqrt{s} = 8$ TeV for each production mode. The ggF and VBF processes are calculated in complex-pole-scheme (CPS), while other WH/ZH and ttH processes are calculated in zero-width-approximation (ZWA).

a wide variety of different experiments. The accuracy on those data can introduce uncertainty on PDF calculation. In addition, strong coupling constant α_s is used in DGLAP evolution [ref] to the higher Q^2 region. Thus, its uncertainty also contributes to the total cross section. There are other uncertainties due to the EW corrections, the different choice of top and bottom quark masses, and the use of large- m_T method. But, the effect to the hadronic cross section is less than a few percent [?] for ggF.

Figure 1.4 shows the hadronic cross sections as a function of m_H for SM Higgs production and uncertainty in different production modes. The ggF and VBF cross sections are based on complex-pole-scheme (CPS), while VH and ttH

ones are based on zero-width-approximation (ZWA). The order of QCD and EW

process	QCD	EW
$pp \rightarrow H$	NNLO	NLO
$pp \rightarrow qqH$	NNLO	NLO
$pp \rightarrow WH$	NNLO	NLO
$pp \rightarrow ZH$	NNLO	NLO
$pp \rightarrow ttH$	NLO	

Table 1.2: The order of QCD and EW calculations.

calculations are summarized in Table 1.2.1. The uncertainty is linear combination of uncertainties from QCD scale variation and PDF+ α_S . At $m_H = 125$ GeV ggH contributes $\sim 87\%$ to the total cross section.

1.2.2 Decay of Higgs Boson

The interaction term in the Lagrangian shows that the Higgs can couple to a pair of weak bosons(VV). Thus, Higgs decays into W^+W^- and ZZ . Depending on the mass of Higgs, one or two of the bosons can be off-shell. Thus we consider three cases where both of them are on-shell(VV), one is on-shell and the other is off-shell(VV^*), and both of them are off-shell(V^*V^*).

- Both bosons are on-shell($H \rightarrow VV$) [ref] :

$$\Gamma(H \rightarrow VV) = \frac{G_F m_H^3}{16\sqrt{2}\pi} \delta_V \sqrt{1 - 4\epsilon^2} (1 - 4\epsilon^2 - 12\epsilon^4) \quad (1.30)$$

where $\epsilon = \frac{M_V}{m_H}$ and $\delta_W = 2$ and $\delta_Z = 1$. The ratio of longitudinal polarization is given by [1]

$$R_L = \frac{\Gamma_L}{\Gamma_T + \Gamma_L} = \frac{1 - 4\epsilon^2 - 4\epsilon^4}{1 - 4\epsilon^2 - 12\epsilon^4} \xrightarrow{\epsilon \rightarrow 0} 1 \quad (1.31)$$

Thus, vector bosons are longitudinally polarized at high m_H ($\epsilon \rightarrow 0$). At the production threshold, $m_H = 2M_V \rightarrow \epsilon = \frac{1}{2}$, R_L is 2 which means that longitudinal and transverse polarizations are equally populated. In addition, the decay width to WW is reduced to

$$\Gamma(H \rightarrow WW) \rightarrow \frac{G_F m_H^3}{16\sqrt{2}\pi} \times 2 \quad (1.32)$$

$$= 2 \frac{1.16637 \times 10^{-5} \text{ GeV}^{-2} m_H^3}{16\sqrt{2}\pi} \quad (1.33)$$

$$\approx 0.33 m_H \times \frac{m_H^2}{\text{TeV}^2} (\text{TeV}). \quad (1.34)$$

For example, at $m_H = 1 \text{ TeV}$, decay width for WW is 0.33 TeV. Practically it is hard to claim a Higgs resonance at high mass regions.

- one is on-shell and the other is off-shell ($H \rightarrow VV^* \rightarrow V f \bar{f}$) where f does not include top quark [ref] :

$$\Gamma(H \rightarrow VV^*) = \frac{3G_F^2 M_v^4}{16\pi^3} m_H \delta'_V R(\epsilon) \quad (1.35)$$

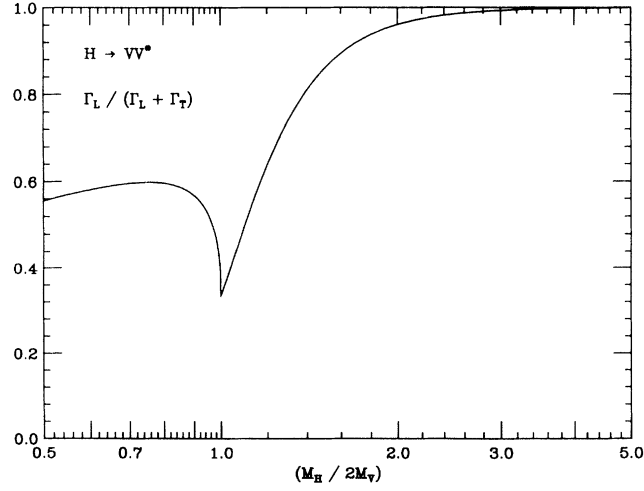


Figure 1.5: The ratio of longitudinal polarization of vector bosons as a function of $\frac{m_H}{2M_V}$ [1]

where $\delta'_W = 1$, $\delta'_Z = \frac{7}{12} - \frac{10}{9} \sin^2 \theta_W + \frac{40}{9} \sin^4 \theta_W$, and

$$Rf(\epsilon) = \frac{3(1 - 8\epsilon^2 + 20\epsilon^4)}{(4\epsilon^2 - 1)^{1/2}} \arccos\left(\frac{3\epsilon^2 - 1}{2\epsilon^3}\right) - (1 - \epsilon^2) \left(\frac{47}{2} \epsilon^2 - \frac{13}{2} + \frac{1}{\epsilon^2} \right) - 3(1 - 6\epsilon^2 + 4\epsilon^4) \ln \epsilon \quad (1.36)$$

The ratio of longitudinal polarization is given [1] by

$$R_L = \frac{\Gamma_L}{\Gamma_T + \Gamma_L} = \frac{R_L(\epsilon)}{R(\epsilon)} \quad (1.37)$$

where R_L is [1]

$$R_L(\epsilon) = \frac{3(1 - 16\epsilon^2 + 20\epsilon^4)}{(4\epsilon^2 - 1)^{1/2}} \arccos\left(\frac{3\epsilon^2 - 1}{2\epsilon^3}\right) - (1 - \epsilon^2) \left(\frac{15}{2} \epsilon^2 - \frac{13}{2} + \frac{1}{\epsilon^2} \right) - (3 - 10\epsilon^2 + 4\epsilon^4) \ln \epsilon. \quad (1.38)$$

Figure 1.5 shows the ratio of longitudinally polarized vector bosons as a function of $\frac{m_H}{2M_V}$ ($=\frac{\epsilon}{2}$). The ratio changes as m_H changes. Thus, we expect event kinematics differs with different m_H hypotheses. This is important when we define signal regions optimized at a given m_H hypothesis. mention $\Delta\phi_{ll}$ here? What does it mean that Vs are transversely polarized? (schemetically)

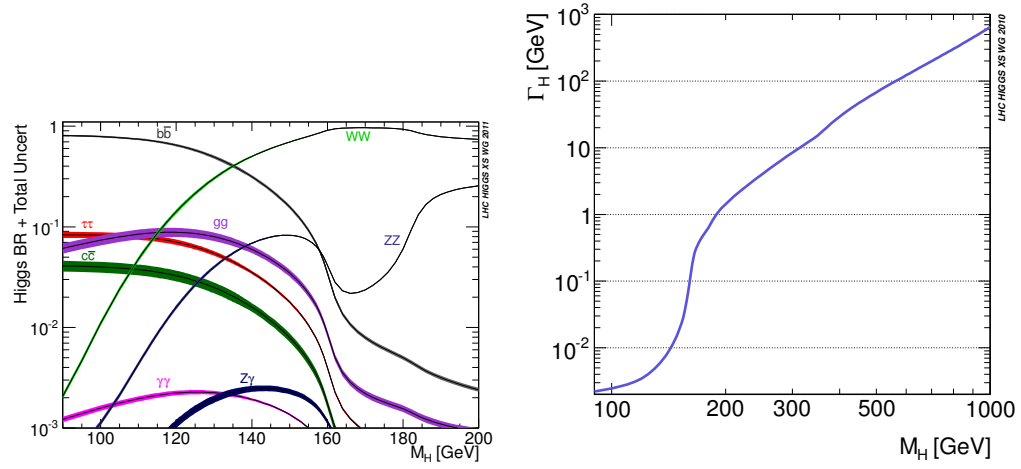


Figure 1.6: Standard Model Higgs boson decay branching ratios at low m_H (left) and total width (right).

Figure 1.6 shows the branching ratios of Standard Model Higgs boson and its total decay width. Top and bottom quarks are included in the calculation. Uncertainties are from ...

Figure 1.7 shows $\sigma \times BR$ at low m_H .

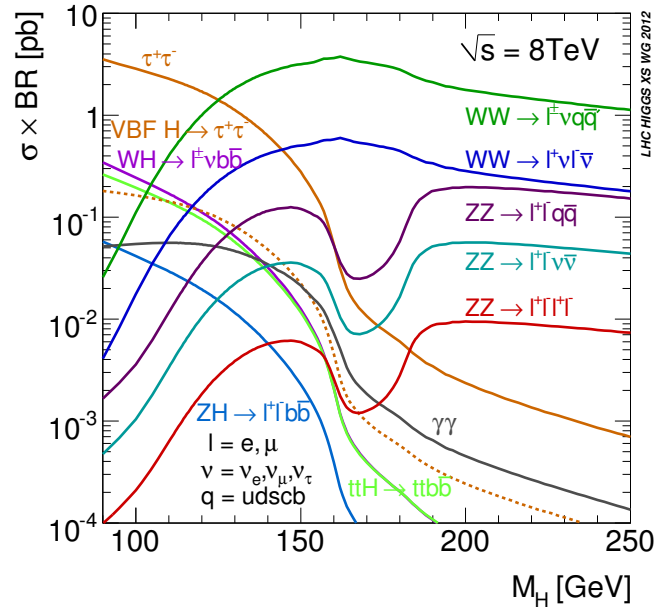


Figure 1.7: $\sigma \times BR$ at low m_H .

1.3 Limits on Higgs Boson Mass

1.3.1 Theoretical Limits

Perturbative Unitarity : $W_L^+ W_L^- \rightarrow W_L^+ W_L^-$

The cross section of longitudinal vector boson scattering, $V_L V_L \rightarrow V_L V_L$, increases as the energy increases, which eventually violate unitarity. This will be discussed in this subsection taking $W_L^+ W_L^- \rightarrow W_L^+ W_L^-$ as an example. Fig. 1.8 shows Feynman diagrams for this process. In the high energy limit $s \gg m_W^2$, the scattering amplitude is [2]

$$\mathcal{A}(W_L^+ W_L^- \rightarrow W_L^+ W_L^-) \sim -\frac{1}{v^2} \left(-s - t + \frac{s^2}{s - m_H^2} + \frac{t^2}{t - m_H^2} \right). \quad (1.39)$$

What does the point diagram correspond to in this equation? According to the Electroweak Equivalence Theorem [?] which says that at very high energy the longitudinal vector bosons can be replaced by their associated Goldstone bosons.

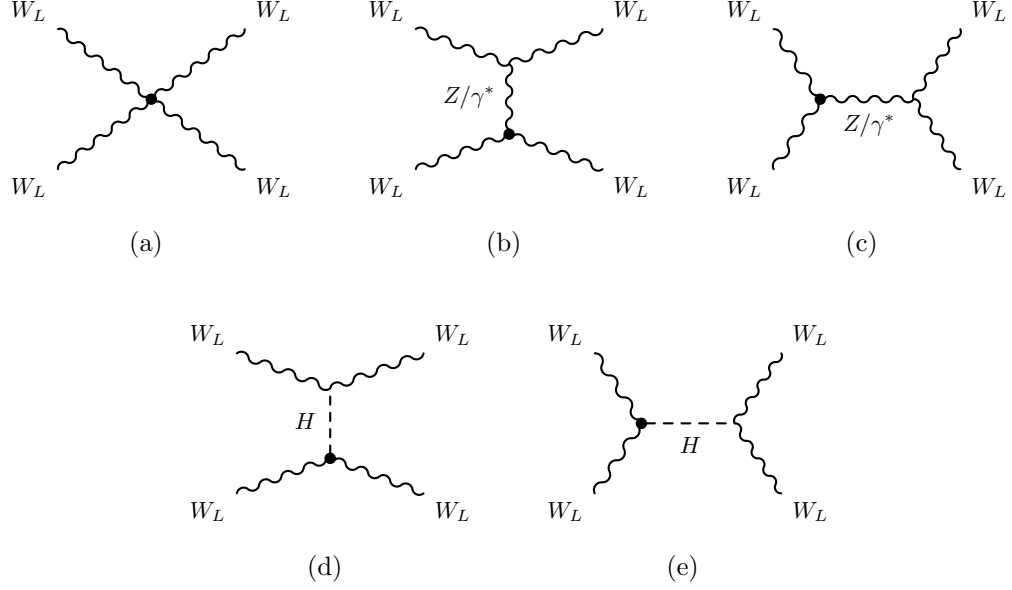


Figure 1.8: Feynman diagrams for $W_L^+ W_L^- \rightarrow W_L^+ W_L^-$ scattering.

Thus, the scattering amplitude can be written using Goldstone bosons (w^\pm)

$$\mathcal{A}(w^+ w^- \rightarrow w^+ w^-) = -\frac{m_H^2}{v^2} \left(2 + \frac{m_H^2}{s - m_H^2} + \frac{m_H^2}{t - m_H^2} \right). \quad (1.40)$$

An scattering amplitude can be decomposed into partial waves a_l

$$\mathcal{A} = 16\pi \sum_{l=0}^{\infty} (2l+1) P_l(\cos \theta) a_l \quad (1.41)$$

where P_l is the Legendre polynomials and θ is the scattering angle. For $2 \rightarrow 2$ cross section using Optical theorem [?], we have the following identity on cross section (σ)

$$\sigma = \frac{16\pi}{s} \sum_{l=0}^{\infty} (2l+1) |a_l|^2 = \frac{1}{s} \text{Im}[\mathcal{A}(\theta=0)] \quad (1.42)$$

which gives the unitary condition,

$$|a_l|^2 = \text{Im}(a_l) \quad \Rightarrow \quad \text{Re}(a_l)^2 + \left[\text{Im}(a_l) - \frac{1}{2} \right]^2 = \left(\frac{1}{2} \right)^2 \quad (1.43)$$

$$\Rightarrow \quad |\text{Re}(a_l)| < \frac{1}{2}. \quad (1.44)$$

Then, the $l = 0$ amplitude in the limit of $s \gg m_H^2$ becomes

$$a_0(w^+w^- \rightarrow w^+w^-) = -\frac{m_H^2}{16\pi v^2} \left[2 + \frac{m_H^2}{s - m_H^2} - \frac{m_H^2}{s} \log \left(1 + \frac{s}{m_H^2} \right) \right] \quad (1.45)$$

$$\rightarrow -\frac{m_H^2}{8\pi v^2} \quad (1.46)$$

The unitary condition (Eq. (1.44)) gives upper bound on m_H ,

$$|Re(a_0)| = \frac{m_H^2}{8\pi v^2} < \frac{1}{2} \quad (1.47)$$

$$\Rightarrow m_H < 2\sqrt{\pi}v \simeq 870 \text{ GeV}. \quad (1.48)$$

Including other scattering channels,

$$Z_L Z_L, HH, Z_L H, W_L^+ H, W_L^+ Z_L \quad (1.49)$$

the constraint on m_H becomes tighter [2],

$$m_H < 710 \text{ GeV}. \quad (1.50)$$

This means that in SM unitarity will be violated if $m_H > 710 \text{ GeV}$ unless there is a new physics that recovers it. So far we calculated only tree-level terms, so we can expect that adding higher order terms can solve this problem. But, including higher order terms does not guarantee that the unitarity will be restored because in the high m_H regime coupling to Higgs is too large and perturbative calculation breaks down. Thus, the mass bound given in eq. 1.50 can be considered the m_H regime where perturbative calculation is reliable in all s .

Triviality and Stability bounds

The variation of the Higgs quartic coupling λ is described by Renormalization Group Equation (RGE). When we consider one-loop radiation correction by Higgs boson itself to λ which are shown in the Fig.1.9, the corresponding RGE is given by [2]

$$\frac{d}{dQ^2} \lambda(Q^2) = \frac{3}{4\pi^2} \lambda^2(Q^2) + \text{higher orders} \quad (1.51)$$

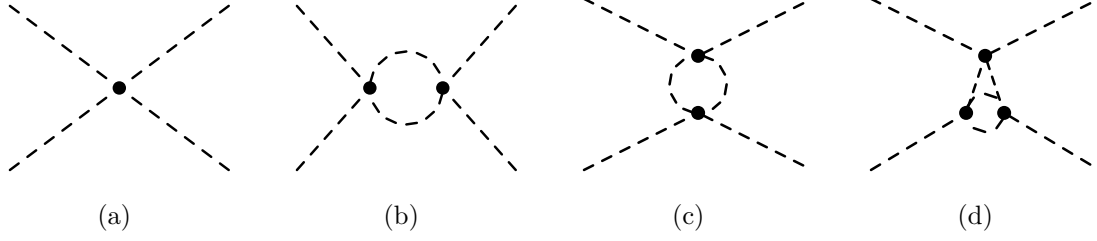


Figure 1.9: Feynman diagrams for Higgs boson quartic interaction. Left is tree level and the right three are one-loop correction by Higgs boson itself.

The solution to this equation is given by

$$\lambda(Q^2) = \frac{\lambda(v^2)}{\left[1 - \frac{3}{4\pi^2}\lambda(v^2)\log\frac{Q^2}{v^2}\right]} \quad (1.52)$$

where the EWSB scale is used as a reference energy point, $Q_0 = v$. If the energy is much smaller than the EWSB scale, $Q^2 \ll v^2$, the quadratic coupling goes to 0, and the theory is called “trivial”, which means that there is no interaction. On the otherhand, if the energy is much larger than the EWSB scale, $Q^2 \gg v^2$, as Q increases the coupling will be infinite at a certain energy scale, Λ_{cut} . Using $\lambda = m_H^2/2v^2$ and the definition of λ that it is positive, we have the following equation for denominator,

$$1 > \frac{3}{4\pi^2} \frac{m_H^2}{2v^2} \log \frac{\Lambda_{cut}^2}{v^2} \quad \Rightarrow \quad m_H^2 > \frac{8\pi^2 v^2}{\log \frac{\Lambda_{cut}^2}{v^2}}, \quad (1.53)$$

which gives a scale-dependent bound on m_H . Imposing $\Lambda_{cut} = m_H$ in which case the theory is not reliable, i.e. valid scale of theory is same as the mass of a particle, the bound on the Higgs mass is $m_H < 640$ GeV. This result is consistent with the limit from unitarity constraint.

In the previous discussion, only was one-loop correction by Higgs itself considered. This is a proper approximation when λ is large. But, in other cases where λ is small, we need to consider the contributions from fermions and vector bosons. Since, the strength of interaction with Higgs boson is proportional to the particle mass, we consider only heavy particles, vector bosons and top quarks. In the limit of small Higgs quartic couplings, $\lambda \ll \lambda_t, g_1, g_2$ where λ_t is the top Yukawa

coupling given by $\sqrt{2}m_t/v$, the RGE is given by [2]

$$\frac{d}{dQ^2}\lambda(Q^2) \simeq \frac{1}{16\pi^2} \left[-12\frac{m_t^4}{v^4} + \frac{3}{16} \left(2g_2^4 + (g_2^2 + g_1^2)^2 \right) \right]. \quad (1.54)$$

Taking EWSB scale as the reference point, the solution to Eq. (1.54) is

$$\lambda(Q^2) = \lambda(v^2) + \frac{1}{16\pi^2} \left[-12\frac{m_t^4}{v^4} + \frac{3}{16} \left(2g_2^4 + (g_2^2 + g_1^2)^2 \right) \right] \log \frac{Q^2}{v^2}. \quad (1.55)$$

As $\lambda(v^2)$ becomes small, the coupling can go negative, leading the vacuum unstable. Thus, in order to maintain the stability of vacuum, $\lambda(Q^2)$ should be positive. This requirement gives

$$m_H^2 > \frac{v^2}{8\pi^2} \left[-12\frac{m_t^4}{v^4} + \frac{3}{16} \left(2g_2^4 + (g_2^2 + g_1^2)^2 \right) \right] \log \frac{\Lambda_{cut}^2}{v^2} \quad (1.56)$$

$$= \frac{v^2}{8\pi^2} \left[-12\frac{m_t^4}{v^4} + \frac{3}{16} \left(2g_2^4 + (g_2^2 + g_1^2)^2 \right) \right] \log \frac{\Lambda_{cut}^2}{v^2} \quad (1.57)$$

$$= \text{work on this line} \quad (1.58)$$

So far the higher order contributions were taken up to 1-loop corrections. There are calculations upto 2-loops and Fig. 1.10 shows lower bound (vacuum stability) and upper bound (triviality) of m_H as a function of new cutoff scale, Λ_{cut} .

Fine tuning

The 1-loop radiative corrections to Higgs mass when only are W/Z/H and top contributions considered is given by [2]

$$m_H^2 = (m_H^0)^2 + \frac{3\Lambda_{UV}^2}{8\pi^2 v^2} [m_H^2 + 2m_W^2 + m_Z^2 - 4m_t^2] \quad (1.59)$$

where m_H^0 is the fundamental parameter of SM and Λ_{UV} is the UV cutoff scale. Therefore, unless Λ_{UV} is in the same scale of EWSB(100 GeV – 1 TeV), there should be an incredible fine-tuning between m_H^0 and the radiative correction to get m_H in EWSB scale. For a quantitative discussion, we first need to define what fine-tuning means. Fine-tuning is defined as the sensitivity of the weak scale to the cutoff, $|\delta m_W^2(\Lambda_{UV})/m_W^2|$, where δm_W^2 is the difference between the tree and

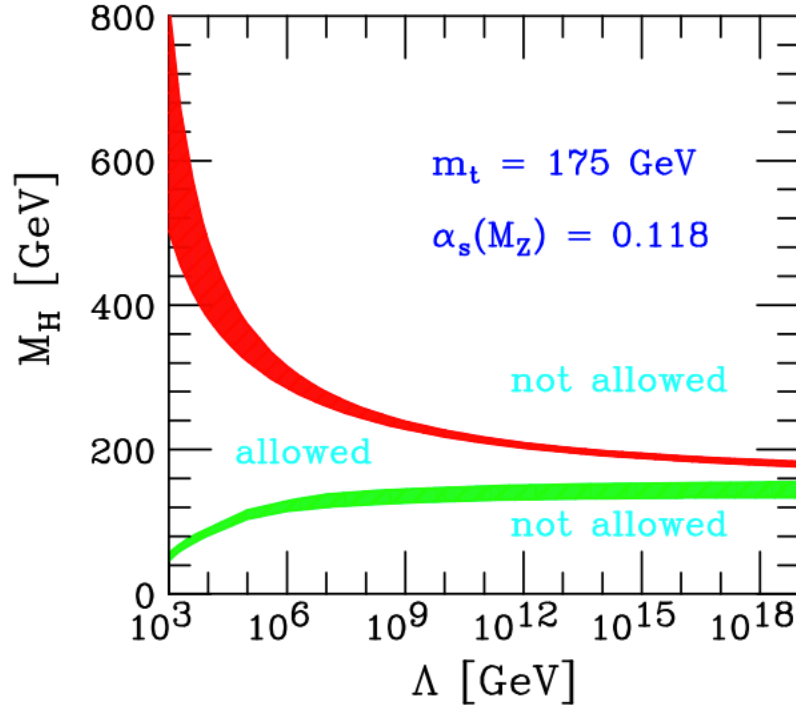


Figure 1.10: Upper and lower bound of m_H as a function of Λ_{cut} .

loop values, with all other quantities held fixed [3]. So, the metric, \mathcal{F} , is

$$\mathcal{F} = \left| \frac{\delta m_W^2}{m_W^2} \right| = \left| \frac{\delta v^2}{v^2} \right| = \left| \frac{\delta \mu^2}{\mu^2} \right| = \left| \frac{\delta m_H^2}{m_H^2} \right| = \frac{2\Lambda^2}{m_H^2} \left| \sum_n \log^2 \left(\frac{\Lambda_{UV}}{m_H} \right) \right| \quad (1.60)$$

and $\mathcal{F} \leq 1$ represents that there is no fine-tuning. The fig. 1.11 [3] shows two regions in $[\Lambda, m_H]$ plane where Λ is the UV cutoff scale, Λ_{UV} ; $\mathcal{F} > 10$ in light-hatching labeled as 10 % and $\mathcal{F} > 100$ in thick-hatching labeled as 1 %. In case of light Higgs scenario, the fine-tuning is even at the low energy scale. For example, at $m_H=130$ GeV the fine-tuning of $\mathcal{F} > 10$ (10 %) requires $\Lambda < 2.3$ TeV. This means that new physics should exist in the regime where LHC experiments can probe.

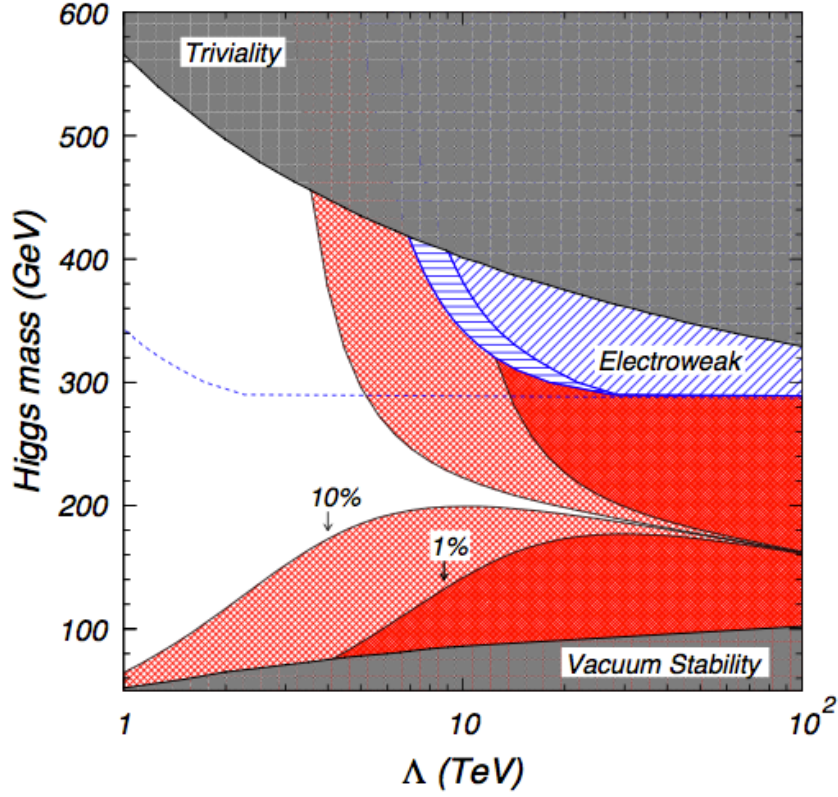


Figure 1.11: Constraint contour from fine tuning, vacuum stability, and triviality

1.3.2 Experimental Limits

Indirect search

There are EWK measurements that are dependent on m_H . For example, the mass of W boson has one-loop correction of Higgs boson as shown in Fig. 1.12. Its contribution to the W mass is parametrized by Δr in the following equation

$$m_W^2 = \frac{\pi\alpha}{\sqrt{2}G_F} \frac{1}{\left(1 - \frac{m_W^2}{m_Z^2}\right)} (1 + \Delta r), \quad (1.61)$$

and the correction is

$$\Delta r \simeq \frac{G_F m_W^2}{8\sqrt{2}\pi^2} \frac{11}{3} \left(\log \frac{m_H^2}{m_W^2} - \frac{5}{6} \right) \quad (1.62)$$

which is dependent on m_H logarithmically. Thus, by measuring other quantities in the equation, we can constrain m_H up to the uncertainties to the measured

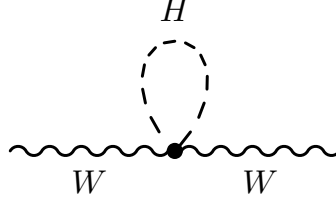


Figure 1.12: Feynman diagram for 1 loop correction by Higgs boson to the W propagator.

quantities. Going one step further, we can use more variables, not only m_W , and put them into a statistical fit [4]. A simultaneous fit is done to $\Delta\alpha_{had}^{(5)}(m_Z^2)$, $\alpha_S(m_Z^2)$, m_Z , m_t , and $\log_{10}(m_H)$ on the data collected by LEP-I/II, SLD, and Tevatron [4]. The fig. 1.13 shows $\Delta\chi^2$ curve from EWK precision measurements assuming that Standard Model is the true theory of nature [4]. The preferred m_H is 94_{-24}^{+29} GeV. It also shows that the upper limit on m_H at C.L. = 95 % is 152 GeV.

Direct search

Before 2012, there were direct searches for SM Higgs boson by LEP, Tevatron, and LHC experiments. The LEP data showed upper limit of $m_H < 114.4$ GeV at $CL_s = 95\%$ [5] and the Tevatron showed exclusion of SM Higgs hypothesis in the range of $147 \text{ GeV} < m_H < 179 \text{ GeV}$ at $CL_s = 95\%$ [5]. At the end of 2011, the LHC experiments (CMS and ATLAS) showed their 7 TeV results on the standard model Higgs search [6, 7]. Fig. 1.14 shows the 95% C.L. upper limits on σ/σ_{SM} as a function of m_H in the range of 110 - 145 GeV for CMS on the left and 110 - 150 GeV for ATLAS on the right. In both experiments, search was performed up to $m_H = 600$ GeV, but only low m_H region is shown on the plots. In CMS, the observed exclusion range is 118 - 543 GeV with expected exclusion range is 127 - 600 GeV. In ATLAS, the observed exclusion range is 112.9 - 115.5, 131-238, and 251-466 GeV with expected exclusion range 124 - 519 GeV. Both experiments, CMS and ATLAS, show local excess of 3.1σ and 3.5σ , respectively, around $m_H = 125$ GeV.

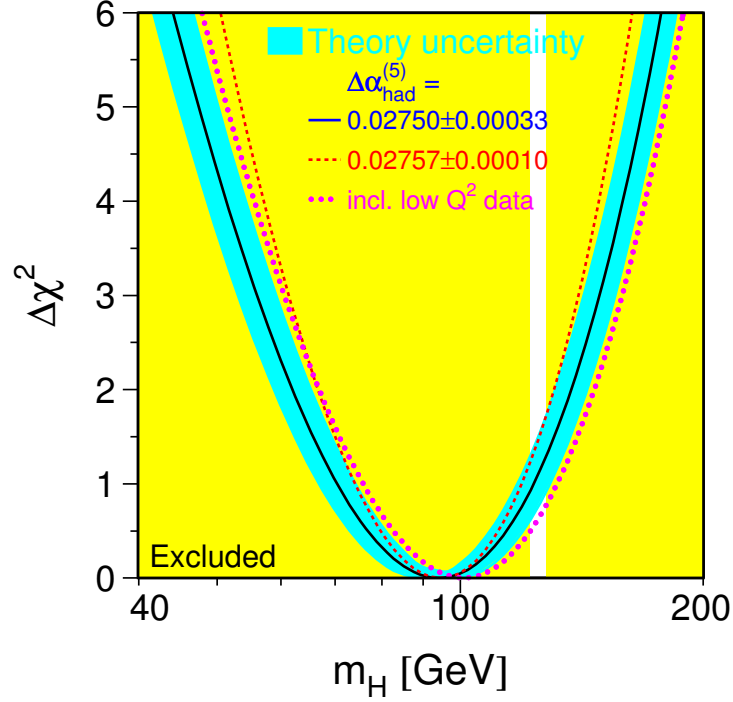


Figure 1.13: blah

1.4 $H \rightarrow W^+W^- \rightarrow 2l2\nu$

1.4.1 Large expected signal yields

As seen in the previous section, the $\sigma \times \text{BR}$ of $H \rightarrow W^+W^- \rightarrow 2l2\nu$ channel is large compared to the other sensitive channels, $H \rightarrow ZZ \rightarrow 4l$ and $H \rightarrow \gamma\gamma$. Table 1.4.1 shows $\sigma \times \text{BR}$ for the most sensitive channels, $H \rightarrow W^+W^- \rightarrow 2l2\nu$,

	$H \rightarrow WW \rightarrow 2l2\nu$	$H \rightarrow ZZ \rightarrow 4l$	$H \rightarrow \gamma\gamma$
$\sigma \times \text{BR}(pb)$	2.24×10^{-1}	2.79×10^{-3}	5.09×10^{-2}
N_{expected} in $\mathcal{L}_{\text{int}} = 20 \text{ fb}^{-1}$	4480	56	1018

Table 1.3: $\sigma \times \text{BR}$ at $m_H = 125 \text{ GeV}$ for most sensitive channels and the expected number of events in $\mathcal{L}_{\text{int}} = 20 \text{ fb}^{-1}$. l means electrons or muons.

$H \rightarrow ZZ \rightarrow 4l$, and $H \rightarrow \gamma\gamma$ and the expected signal events at the integrated

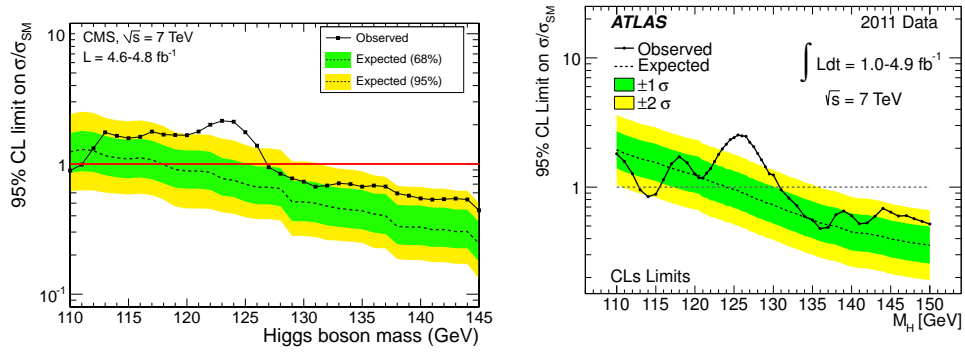


Figure 1.14: CMS / ATLAS Higgs exclusion with 7 TeV data.

luminosity, $\mathcal{L} = 20 \text{ fb}^{-1}$. The expected signal events are 4480, 56, and 1018, respectively. This allows to have a good statistical power to measure the cross section (signal strength) with this channel.

1.4.2 Angular distribution of leptons in the final state

The spin of SM Higgs is zero, so by helicity conservation the total spin of the WW system should be zero. As shown in Fig. 1.15, if we take the direction

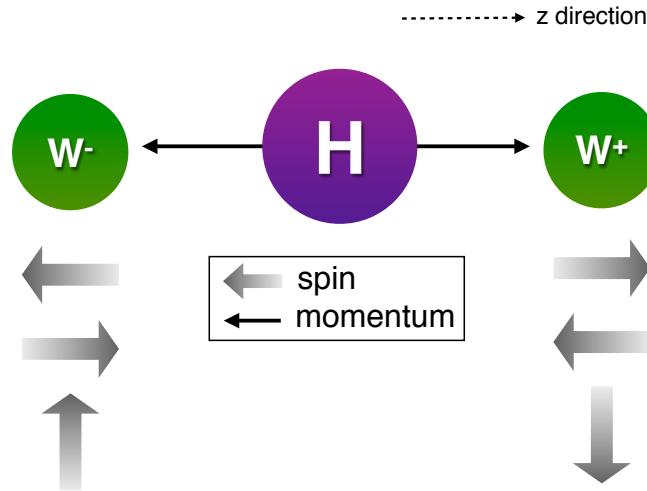


Figure 1.15: blah

of W^+ momentum as z axis in the CM of Higgs, there are two cases where the spin direction is parallel to the momentum direction (transverse polarization) and one case where it is perpendicular to the momentum direction (longitudinal polarization). In case of transverse polarization, the leptons from Ws have strong angular dependence due to V-A nature of weak decays, i.e. neutrinos are always left-handed (anti-neutrinos are always right-handed). Let's take the case of W^+ spin in the z direction as an example. In order for the neutrino from W^+ to be left-handed, the direction of the neutrino should be in the - z direction, thus lepton should fly to z direction. In order for the anti-neutrino from W^- to be right-handed, the direction of the anti-neutrino should be in the - z direction, thus lepton should fly to z direction. Therefore, both leptons tend to move in the same direction resulting the angle between the two leptons to be small. This is somewhat diluted due to boost of Higgs and Ws, but the effect is still visible and used to separate signals from non-resonant WW background. On the other hand, in case of longitudinal polarization, no specific angular correlation is present.

1.4.3 Kinematic variables

Figure 1.16 shows distributions of kinematic variables for multiple Higgs hypotheses, $m_H = 110, 125, 145, 160, ,$ and 200 GeV. The plotted variables are leading and trailing lepton p_T , azimuthal angle difference between the two leptons $\Delta\phi_{\ell\ell}$, di-lepton invariant mass $m_{\ell\ell}$, and Higgs transverse mass m_T which is defined as

$$m_T = \sqrt{2p_T^{\ell\ell} E_T^{\text{miss}} (1 - \cos(\Delta\phi_{\ell\ell-E_T^{\text{miss}}}))} \quad (1.63)$$

where p_T is transverse momentum of the dilepton system, E_T^{miss} is missing transverse momentum, and $\Delta\phi_{\ell\ell-E_T^{\text{miss}}}$ is the angle between dilepton direction and E_T^{miss} in the transverse plane. The most of events have leading lepton $p_T^{\ell, \text{max}}$ greater than 20 GeV for all m_H hypotheses. The trailing lepton $p_T^{\ell, \text{min}}$ is quite populated at low $p_T^{\ell, \text{min}}$ region, especially for low m_H hypotheses. In case of $m_H = 125$ GeV, approximately 25 % of events are rejected by requiring $p_T^{\ell, \text{min}} > 10$ GeV. The $\Delta\phi_{\ell\ell}$, azimuthal angle difference between the two leptons, shows non-

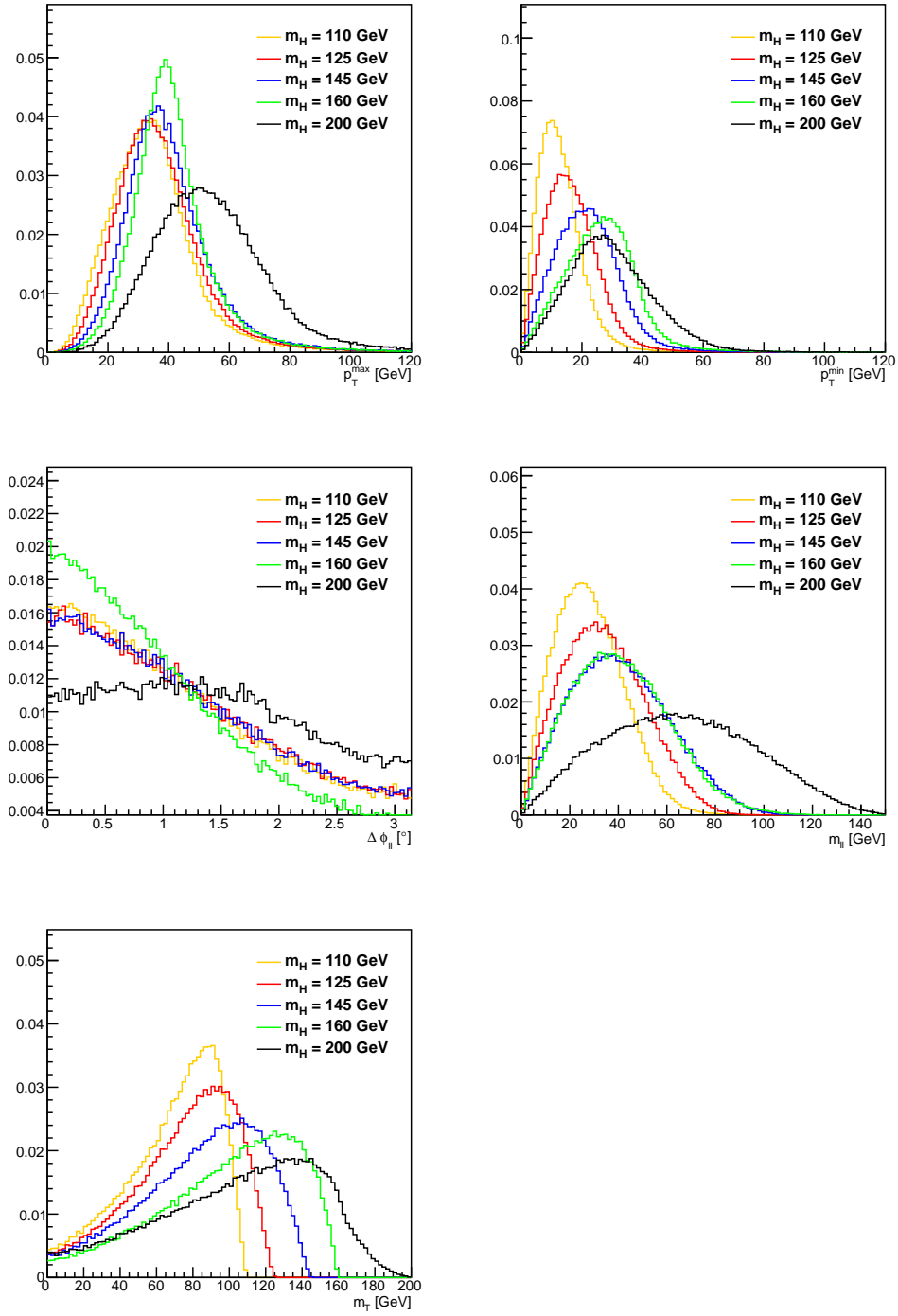


Figure 1.16: blah

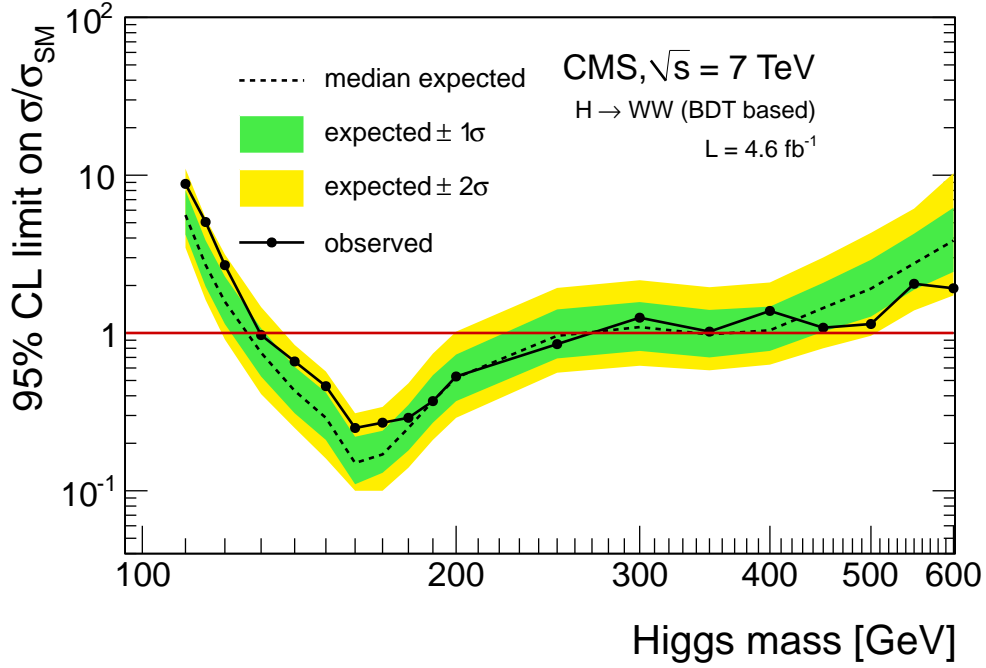


Figure 1.17: Exclusion limit of SM Higgs with 2011 data($\sqrt{s} = 7$ TeV, $\mathcal{L} = 4.6 \text{ fb}^{-1}$). The observed(expected) exclusion limit at CL = 95 % is $m_H = 129 - 270(127 - 270)$ GeV.

straightforward trend. The angle tends to get smaller as m_H increases up to 160 GeV, and the angle becomes wide after $m_H = 160$ GeV. This behavior was expected in the fig. 1.5 where the fraction of the longitudinal polarization is at the minimum at $m_H = 2m_W$ which is about 160 GeV. Since small $\Delta\phi_{\ell\ell}$ yields small $m_{\ell\ell}$, we expect small $m_{\ell\ell}$ for low m_H hypotheses. The Higgs transverse mass m_T shows clear drop at m_H **why tail and lazy drop at 200 GeV?**,

1.4.4 CMS HWW results as of 2011

Before 2012, 4.6 fb^{-1} of data at $\sqrt{s} = 7$ TeV collected by CMS detector was analyzed for SM Higgs search [8]. Figure 1.17 shows exclusion limit using the state-of-the-art analysis technique at the time of study. The observed exclusion limit at $CL_s = 95\%$ is $m_H = 129 - 270$ GeV with expected limit $m_H = 127 - 270$ GeV.

Chapter 2

LHC and CMS Detector

2.1 Large Hadron Collider

Overview of accelerator * How protons are generated * Steps to get accelerated * Luminosity determination

2.2 Compact Muon Solenoid detector

2.2.1 Tracker : pixel and silicon detector

2.2.2 ECAL

2.2.3 HCAL

2.2.4 Magnet

2.2.5 Muon System

2.2.6 Forward : HF

2.2.7 Computing : grid computing

Chapter 3

Event Reconstruction and Selection

Discuss how basic objects(vertex, electron, muon, jet, MET, top-tagging) are reconstructed and what selections are. Other selections will be discussed in the next chapter, Signal Extraction.

3.1 Trigger

- list of triggers
- what are the requirements : already in AN

As seen in section 1.4.3, $H \rightarrow W^+W^- \rightarrow 2l2\nu$ events have trailing lepton whose transverse momentum goes down very low for low m_H hypotheses. Triggering low p_T leptons is very challenging because of large background events. Therefore, in order to record signal events, we need to trigger on the leading lepton, or on both leptons. The leading lepton option is not possible because the identification and isolation requirements should be very tight and momentum thresholds should be very high to maintain sustainable bandwidth. Thus, we trigger on the both leptons. The double-lepton triggers we designed for this analysis have high efficiency for signal events, but are loose enough to collect events in the several control regions we used for various studies. We also use control region triggers that allow fake rate and lepton selection efficiency measurements with the precision good enough for this analysis.

Where can I check the bandwidth of triggers? want to know the total bandwidth of CMS and the bandwidth of triggers we use

3.1.1 Analysis Triggers

The double-lepton triggers that are listed in Table 3.1 require two HLT objects and each of them is required to match an L1 seed. The offline lepton p_T requirement is 20/10 GeV, so the online lepton p_T requirement is a bit looser, 17/8 GeV, in order to be safe from possible tighter online selection. In addition, the longitudinal distance between the two vertices of the leptons is required to be less than 0.2 cm in order to reduce Pile-Up events.

For electron HLT objects there are additional requirements on shower shapes, track-to-cluster matching, track/calorimeter isolation. The exact variables and cut values are described in Table 3.3. In the table, the naming convention of CMS HLT triggers are shown with the corresponding requirements. H/E is the ratio of energy deposit in HCAL to that of ECAL. $\sigma_{\eta\eta}$ is the weighted sum of η difference between the seed crystal and the 5x5 crystals surrounding the it. $|\Delta\eta|(|\Delta\phi|)$ is the difference in absolute value between the center of the supercluster and the direction of the track trajectory in $\eta(\phi)$ direction. $|\frac{1}{E} - \frac{1}{p}|$ is the difference between the reciprocal of supercluster energy and the reciprocal of the track momentum. E_{CallIso}/E_T , H_{CallIso}/E_T , and TrkIso/E_T are the sum of the trasverse energy within $dR < 0.3$ (checked) around the center of energy deposit or track trajectory divided by the transverse energy, E_T . Because simplified algorithm is used for online variables, the variables do not exactly correspond to the offline ones. To account for this, we measure tirgger efficiency with respect to the offline selection and do corrections accordingly. The details on this can be found in 4.1.3 where trigger efficiency measurement is discussed. **what is TkMu8? what is the iso requirement on single muon triggers?**

Double-lepton trigger name	L1 seed
HLT_Ele17_CaloIdT_CaloIsoVL_TrkIdVL_TrkIsoVL_Ele8_CaloIdT_CaloIsoVL_TrkIdVL_TrkIsoVL_v[15-19]	L1_DoubleEG_13_7
HLT_Mu17_Mu8_v[16-22] HLT_Mu17_TkMu8_v[9-14]	L1_DoubleMu_10_Open OR L1_DoubleMu_10_3p5
HLT_Mu17_Ele8_CaloIdT_CaloIsoVL_TrkIdVL_TrkIsoVL_v[4-9] HLT_Mu8_Ele17_CaloIdT_CaloIsoVL_TrkIdVL_TrkIsoVL_v[4-9]	L1_Mu12_EG7 L1_MuOpen_EG12 OR L1_Mu3p5_EG12

Table 3.1: Double-lepton triggers used to collect signal events.

Single-lepton trigger name	L1 seed
HLT_Ele27_WP80_v[8-11]	L1_SingleEG20 OR L1_SingleEG22
HLT_IsoMu24_eta2p1_v[11-15]	L1_SingleMu16er

Table 3.2: Single-lepton triggers used to collect signal events.

name	criterion
CaloId_T	$H/E < 0.15(0.10)$ $\sigma_{\eta\eta} < 0.011 (0.031)$
CaloId_VT	$H/E < 0.05(0.05)$ $\sigma_{\eta\eta} < 0.011 (0.031)$
TrkId_VL	$ \Delta\eta < 0.01 (0.01)$ $ \Delta\phi < 0.15 (0.10)$
TrkId_T	$ \Delta\eta < 0.008 (0.008)$ $ \Delta\phi < 0.07 (0.05)$
CaloIso_VL	$E\text{CalIso}/E_T < 0.2 (0.2)$ $H\text{CalIso}/E_T < 0.2 (0.2)$
CaloIso_T	$E\text{CalIso}/E_T < 0.15 (0.075)$ $H\text{CalIso}/E_T < 0.15 (0.075)$
CaloIso_VT	$E\text{CalIso}/E_T < 0.05 (0.05)$ $H\text{CalIso}/E_T < 0.05 (0.05)$
TrkIso_VL	$\text{TrkIso}/E_T < 0.2 (0.2)$
TrkIso_T	$\text{TrkIso}/E_T < 0.15 (0.075)$
TrkIso_VT	$\text{TrkIso}/E_T < 0.05 (0.05)$
WP80	$H/E < 0.10(0.05)$ $\sigma_{\eta\eta} < 0.01 (0.03)$ $ \Delta\eta < 0.007 (0.007)$ $ \Delta\phi < 0.06 (0.03)$ $ \frac{1}{E} - \frac{1}{p} < 0.05 (0.05)$ $E\text{CalIso}/E_T < 0.15 (0.10)$ $H\text{CalIso}/E_T < 0.10 (0.10)$ $\text{TrkIso}/E_T < 0.05 (0.05)$

Table 3.3: Summary of requirements applied to electrons in the triggers used for this analysis. The selection requirements are given for electrons in the barrel (end-cap). The abbreviation in the names means L=Loose, VL=Very Loose, T=Tight, and VT=Very Tight.

3.1.2 Utility Triggers

The lepton selection efficiency measurements are performed using Tag-And-Probe method on $Z/\gamma^* \rightarrow \ell\ell$ events. In order to use Tag-And-Probe method, we should select pure sample of $Z/\gamma^* \rightarrow \ell\ell$ events to reduce systematics due to selecting non-prompt leptons from other background processes or Pile-Up. Apart from analysis triggers, for this kind of study we do not have to select all events, but pure samples with adequate statistics. The single lepton triggers used to collect

signal events, listed in Table 3.2, can be used to also select $Z/\gamma^* \rightarrow \ell\ell$ events. The leading lepton is likely to be triggered, letting the trailing leptons be unbiased sample of leptons that covers wide range of kinematic region that stretches to the low p_T region.

In order to estimate backgrounds such as W +jets that have a non-prompt lepton that passes the full lepton selection, we use "fake rate" method. The details of this method are discussed in 6.4. In this method we define a looser selection and calculate the ratio of the events that pass the full selection to the events that pass the looser selection using single-lepton events dominated by QCD processes. The ratio is called fake rate. The fake rate differs by event kinematics such as p_T and η of the lepton, and the p_T of the leading jet that recoils off the lepton. Given that the leptons in the data sample collected by the analysis triggers are trigger objects, the tightest possible loose definition is the trigger requirements of the analysis triggers. We devised a set of single-lepton triggers that have the looser or same requirements on leptons as the double-lepton triggers. Note that the single lepton triggers have tighter requirements on leptons. In order to cover large lepton p_T range, we use several triggers with different lepton p_T thresholds. Because the jet p_T distribution is exponentially falling, we need triggers that require corrected leading jet p_T be greater than 30 GeV. These triggers give sufficient samples for systematic study on fake rate method.

3.2 Event Primary Vertex

- Track reconstruction : Kalman Filter, ...
- Vertex reconstruction : vertex finding, vertex fitting, ...
- Primary Vertex selection

The primary vertices are reconstructed by Deterministic Annealing clustering of tracks [?].

The offline primary vertices are required to be within 24 cm from the center of the detector(or beamspot?) in z direction. It should be within 2 cm from the

Trigger name	L1 seed
HLT_Ele8_CaloIdT_TrkIdVL_v[2-5]	L1_SingleEG5
HLT_Ele8_CaloIdT_CaloIsoVL_TrkIdVL_TrkIsoVL_v[12-15]	L1_SingleEG7
HLT_Ele17_CaloIdT_CaloIsoVL_TrkIdVL_TrkIsoVL_v[3-6]	L1_SingleEG12
HLT_Ele8_CaloIdT_CaloIsoVL_TrkIdVL_TrkIsoVL_Jet30_v[3-7]	L1_SingleEG7
HLT_Ele17_CaloIdT_CaloIsoVL_TrkIdVL_TrkIsoVL_Jet30_v[3-7]	L1_SingleEG12
HLT_Mu8_v[16-18]	L1_SingleMu3
HLT_Mu17_v[3-5]	L1_SingleMu12

Table 3.4: Utility triggers for fake rate method and zeta method. The identification and isolation requirements for electrons are described in Table 3.3.

beamspot in the radial direction. The degrees of freedom of the vertex fit should be 4 or larger. **what does this mean exactly?**

At high luminosity collisions, there are multiple proton-proton interactions happening at the same bunch crossing. In those interactions there is usually only one interaction that is of interest for our analysis, that triggered that event. These interactions tend to be associated with energetic objects, while the other interactions are mostly inelastic scatterings that produce soft objects. Therefore, we choose the event primary vertex by selecting the primary vertex with largest scalar sum of p_T^2 of tracks associated the vertex. The vertices of leptons are required to be very close to the event primary vertex.

3.3 Electron

- **Electron reconstruction** : GSF track, seeding, ...
- **ID** : MVA (list of input variables, trainig samples, cut values)
- **ISO** : list of variables to calculate the final cut variable, cut values

Electrons are reconstructed using tracks and energy deposit ECAL. Since

they brem in the tracker, this loss of energy should be taken into account in the reconstruction.

An electron candidate is reconstructed if there is a track and a SC energy deposit compatible with the track momentum. When there is a random combination of a track from π^\pm and a SC energy deposit from π^0 that eventually decays to two photons, a fake electron candidate can be made. In order to suppress them, we apply electron selection which is composed of requirements on identification (track-to-SC matching, track fit quality, shower shape, energy loss due to bremsstrahlung, ratio of hadronic energy to electromagnetic energy), isolation, impact parameter. Other source of fake electrons is a photon conversion to a pair of electron and a positron in the material. If the conversion is asymmetric, *i.e.* one particle carries most of the photon momentum, that particle can be selected as an electron candidate. Thus, we apply additional requirement on the conversion rejection.

For the electron identification we use BDT-based multivariate approach [?]. The training is done with 2011 data; $Z/\gamma^* \rightarrow \ell\ell$ events for signal and QCD-dominated events collected by the fake rate triggers listed in section 3.1. In order to increase the separation by selecting and mitigate possible bias due to triggers, a set of preselection cuts that are as tight as trigger requirements is applied.

In order to suppress the electrons from a conversion from a photon, we reject the electron if there is a reconstructed conversion vertex where one of the two tracks match with the electron, if the probability of the conversion vertex fit is greater than 10^{-6} , What about `cms2.convs_dl()[iconv]> dlMin` ? and there are any missing hits in the electron track before the conversion vertex.

3.4 Muon

- Muon reconstruction : ...
- ID : list variables and cut values
- ISO : MVA (list of input variables, training samples, cut values)

3.5 Jet

- Jet reconstruction : anti-kT ($dR = 0.5$)
- Jet energy correction : L1Fastjet/L2/L3 (+ Residual correction in data)
- lepton veto ($dR > 0.3$)
- MVA jet ID(list of input variables, training samples, cut values)
- two definitions : (1) jet bin counting($p_T > 30$ GeV) (2) top veto($10 < p_T < 30$ GeV)

3.6 Missing Transverse Energy

- How MET(pfMET and trackMET) is calculated
- mention MET ϕ modulation correction
- define projected MET (compare signal and bkgd, (ex) $Z \rightarrow \tau\tau$)
- cut values (minMET > 20 GeV)

3.7 Top-tagging

- How B-tagging algorithm works and working point (TCHEM : Track Counting High Efficiency Medium)
- how the discriminating variable is calculated
- quote some performance plots
- soft-muon tagging requirement

Chapter 4

Efficiency Measurements

4.1 Lepton Efficiency

In collisions events are recorded when the two leptons pass trigger requirements. Thus, per event trigger efficiency needs to be measured using data. To select identified and isolated leptons from Higgs events, we require that each lepton meet strict offline criteria. To account for the possible difference of offline selection efficiencies in simulation and data, we need to measure it in simulation and data separately and apply a scale factors ($\epsilon_{data}/\epsilon_{simulation}$) to simulation.

The efficiencies are measured using Tag-And-Probe method [ref]. We use $Z/\gamma^* \rightarrow e^+e^-$ or $Z/\gamma^* \rightarrow \mu^+\mu^-$ events passing single-lepton trigger to select unbiased, identified and isolated prompt leptons. One lepton which is called "tag" is required to pass the single lepton trigger requirement and the full offline selection. By requiring full selection on the tag, we can enhance the purity of the sample. The other lepton which is called "probe" is required to pass a set of selection criteria that enhances the purity of sample while leaving the criteria under study unbiased. The fact that tag passed single-lepton trigger guarantees that the probe is not biased by trigger. Both legs can be used as a tag in offline efficiency measurement while only can one of them be in trigger efficiency measurement due to the correlation between two offline lepton objects in double-lepton triggers.

The offline selection efficiency is composed of identification(ID) and isolation(ISO) parts. We use N-1 method where ID and ISO efficiencies are measured with respect to the other and multiplied afterwards. When measuring efficiency of ID part (ϵ_{ID}) probe is required to pass full isolation requirement and when measuring efficiency of ISO part (ϵ_{ISO}) probe is required to pass full identification requirement. **mention that eff is measured as a function of pT and eta of lepton** The possible bias due to correlation of the two measurements is estimated by comparing efficiencies measured by N-1 method and combined measurement of ID+ISO efficiency in simulation. The difference which ranges from xx to yy depending on the kinematic bins of a lepton is assigned as systematic uncertainty of the method. **What are the other systematics? For electron, systematics to electron reconstruction efficiency(prob for a SC to be matched to a ECAL-driven GSF electron), 100 +/- 2% (measured with 2011 data). In the code, there are 2 % and**

1.5 % for electron and muon, respectively. Are they from reconstruction efficiency and other ones are negligible compared to these values?

Requiring tight selections to tag and using N-1 method gives high-purity sample of Z/γ^* events in data. However, there are residual contributions from non-prompt leptons from W +jets and QCD events especially at low p_T bins. Thus, we extract yields by fitting the $m_{\ell\ell}$ distribution of the tag and probe pair with Gaussian + exponential \times error function. The Gaussian function which is for Z/γ^* invariant mass peak is modeled by simulation and gaussian smearing is applied to account for difference in lepton momentum resolutions between data and simulation. I don't believe this is true. Looking at the plots with fitted shapes, it seems that there are more than one fit function. need to check in the code. The exponential \times error function is for backgrounds. To allow enough sidebands for backgrounds, $m_{\ell\ell}$ range is chosen to be $60 \text{ GeV} < m_{\ell\ell} < 120 \text{ GeV}$. In case of simulation, efficiencies are calculated by counting events in $81 \text{ GeV} < m_{\ell\ell} < 101 \text{ GeV}$. In simulation, to select leptons from Z/γ^* only (=to remove mis-reconstructed leptons), the dR between probe and the closest, same flavor, generator-level lepton after final-state-radiation(FSR) is required to be within 0.2.

The data/simulation efficiency scale factors per event are then calculated by multiplying per lepton efficiencies measured in data and simulation,

$$\epsilon_{offline}^{event} = \epsilon_{ID}^{lepton1} \times \epsilon_{ISO}^{lepton1} \times \epsilon_{ID}^{lepton2} \times \epsilon_{ISO}^{lepton2}. \quad (4.1)$$

The trigger efficiency($\epsilon_{trigger}$) is measured with respect to the full offline selection. Finally, simulation events are corrected by applying the offline selection scale factor and trigger efficiency,

$$\frac{\epsilon_{offline,MC}^{event}}{\epsilon_{offline,MC}^{event}} \times \epsilon_{trigger}. \quad (4.2)$$

4.1.1 Electron Selection Efficiency

Electron efficiency is composed of two factors, reconstruction efficiency and selection efficiency. The reconstruction efficiency is the probability for a super-cluster energy deposit to be matched to a reconstructed ECAL-driven GSF electron. For this analysis, we use the result measured with 2011 data because new

measurement has not made with the full 2012 data sample[ref]. Really no new study?. The efficiency is measured as a function of p_T and η of a lepton. From the study, we assume that the reconstruction efficiency for an electron is unity with uncertainty at the level of 2 %.

	$0 < \eta < 0.8$	$0.8 < \eta < 1.479$	$1.479 < \eta < 2$	$2 < \eta < 2.5$
N-1 Efficiencies in data				
$10 < p_T < 15$	0.3289 ± 0.0049	0.4353 ± 0.0046	0.1551 ± 0.0040	0.1059 ± 0.0026
$15 < p_T < 20$	0.5981 ± 0.0026	0.6330 ± 0.0028	0.3140 ± 0.0033	0.2379 ± 0.0030
$20 < p_T < 30$	0.7208 ± 0.0009	0.7457 ± 0.0010	0.5147 ± 0.0011	0.4609 ± 0.0021
$30 < p_T < 40$	0.8293 ± 0.0002	0.8481 ± 0.0004	0.6780 ± 0.0015	0.5962 ± 0.0015
$40 < p_T < 50$	0.8623 ± 0.0004	0.8840 ± 0.0005	0.7558 ± 0.0007	0.6573 ± 0.0009
$50 < p_T < 7000$	0.8745 ± 0.0004	0.8936 ± 0.0005	0.7859 ± 0.0012	0.6891 ± 0.0015
N-1 Efficiencies in simulation				
$10 < p_T < 15$	0.4583 ± 0.0055	0.5405 ± 0.0053	0.2267 ± 0.0058	0.1890 ± 0.0056
$15 < p_T < 20$	0.6671 ± 0.0030	0.7126 ± 0.0031	0.3904 ± 0.0045	0.3426 ± 0.0047
$20 < p_T < 30$	0.7594 ± 0.0010	0.7943 ± 0.0011	0.5762 ± 0.0019	0.5090 ± 0.0021
$30 < p_T < 40$	0.8492 ± 0.0005	0.8797 ± 0.0005	0.7215 ± 0.0010	0.6291 ± 0.0012
$40 < p_T < 50$	0.8774 ± 0.0004	0.9091 ± 0.0004	0.7843 ± 0.0007	0.6915 ± 0.0010
$50 < p_T < 7000$	0.8893 ± 0.0007	0.9169 ± 0.0007	0.8039 ± 0.0013	0.7149 ± 0.0017
Simulation-to-data scale factors				
$10 < p_T < 15$	0.7177 ± 0.0138	0.8053 ± 0.0117	0.6842 ± 0.0249	0.5602 ± 0.0214
$15 < p_T < 20$	0.8966 ± 0.0056	0.8882 ± 0.0055	0.8045 ± 0.0126	0.6943 ± 0.0128
$20 < p_T < 30$	0.9491 ± 0.0017	0.9388 ± 0.0019	0.8933 ± 0.0035	0.9056 ± 0.0056
$30 < p_T < 40$	0.9766 ± 0.0006	0.9641 ± 0.0007	0.9396 ± 0.0024	0.9477 ± 0.0030
$40 < p_T < 50$	0.9828 ± 0.0006	0.9724 ± 0.0007	0.9637 ± 0.0013	0.9507 ± 0.0018
$50 < p_T < 7000$	0.9834 ± 0.0009	0.9746 ± 0.0009	0.9776 ± 0.0021	0.9639 ± 0.0032

Table 4.1: HWW Electron V00-02-09 Moriond jae NM1Eff ID

Table 4.1 and 4.2 show electron N-1 efficiencies in data and simulation, and data-to-simulation scale factors for ID and ISO selections, respectively. The scale factors are close to unity except for the low p_T bins for ID efficiency. What is the cause of this?

Table 4.3 shows systematic uncertainty due to use of N-1 method. The uncertainty is estimated by comparing measured efficiencies using N-1 method and the measuring the full (ID and ISO) efficiency at the same time in simulation.

Why it is high at low p_T ? More correlation between ID and ISO at low p_T ?

	$0 < \eta < 0.8$	$0.8 < \eta < 1.479$	$1.479 < \eta < 2$	$2 < \eta < 2.5$
N-1 Efficiencies in data				
$10 < p_T < 15$	0.7827 ± 0.0042	0.7973 ± 0.0029	0.8009 ± 0.0199	0.8546 ± 0.0110
$15 < p_T < 20$	0.8167 ± 0.0007	0.8360 ± 0.0034	0.8155 ± 0.0145	0.8776 ± 0.0041
$20 < p_T < 30$	0.8798 ± 0.0011	0.8815 ± 0.0007	0.8787 ± 0.0017	0.9246 ± 0.0091
$30 < p_T < 40$	0.9391 ± 0.0000	0.9398 ± 0.0007	0.9337 ± 0.0006	0.9598 ± 0.0004
$40 < p_T < 50$	0.9710 ± 0.0001	0.9721 ± 0.0002	0.9704 ± 0.0002	0.9802 ± 0.0002
$50 < p_T < 7000$	0.9816 ± 0.0002	0.9815 ± 0.0008	0.9815 ± 0.0003	0.9873 ± 0.0004
N-1 Efficiencies in simulation				
$10 < p_T < 15$	0.7724 ± 0.0061	0.8015 ± 0.0052	0.7856 ± 0.0109	0.8516 ± 0.0110
$15 < p_T < 20$	0.8214 ± 0.0027	0.8362 ± 0.0028	0.8213 ± 0.0052	0.8761 ± 0.0053
$20 < p_T < 30$	0.8850 ± 0.0008	0.8906 ± 0.0009	0.8768 ± 0.0016	0.9091 ± 0.0017
$30 < p_T < 40$	0.9464 ± 0.0003	0.9473 ± 0.0003	0.9360 ± 0.0006	0.9484 ± 0.0007
$40 < p_T < 50$	0.9757 ± 0.0002	0.9768 ± 0.0002	0.9708 ± 0.0003	0.9720 ± 0.0004
$50 < p_T < 7000$	0.9843 ± 0.0003	0.9842 ± 0.0003	0.9827 ± 0.0005	0.9809 ± 0.0006
Simulation-to-data scale factors				
$10 < p_T < 15$	1.0133 ± 0.0096	0.9948 ± 0.0074	1.0195 ± 0.0290	1.0036 ± 0.0183
$15 < p_T < 20$	0.9943 ± 0.0034	0.9999 ± 0.0053	0.9930 ± 0.0188	1.0017 ± 0.0076
$20 < p_T < 30$	0.9941 ± 0.0016	0.9898 ± 0.0013	1.0021 ± 0.0027	1.0170 ± 0.0102
$30 < p_T < 40$	0.9923 ± 0.0003	0.9921 ± 0.0008	0.9976 ± 0.0009	1.0121 ± 0.0008
$40 < p_T < 50$	0.9951 ± 0.0002	0.9952 ± 0.0003	0.9996 ± 0.0004	1.0084 ± 0.0005
$50 < p_T < 7000$	0.9973 ± 0.0003	0.9973 ± 0.0008	0.9988 ± 0.0005	1.0065 ± 0.0008

Table 4.2: HWW Electron V00-02-09 Moriond jae NM1Eff Iso

	$0 < \eta < 0.8$	$0.8 < \eta < 1.479$	$1.479 < \eta < 2$	$2 < \eta < 2.5$
$10 < p_T < 15$	0.075	0.043	0.089	0.091
$15 < p_T < 20$	0.020	0.018	0.045	0.041
$20 < p_T < 30$	0.005	0.007	0.016	0.006
$30 < p_T < 40$	0.001	0.001	0.003	0.001
$40 < p_T < 50$	0.000	0.000	0.000	0.001
$50 < p_T$	0.000	0.000	0.000	0.000

Table 4.3: The additional systematic uncertainty δ_{SF} on the simulation-to-data scale factor for the electron selection due to the N-1 factorisation scheme.

4.1.2 Muon Selection Efficiency

As in the electron case, muon efficiency is composed of two factors, reconstruction efficiency and selection efficiency. The reconstruction efficiency is the probability for a well-reconstructed track in muon chamber to be matched to a reconstructed track in the inner tracker. For this analysis, we use the result measured with 2011 data because new measurement has not made with the full 2012 data sample[ref]. The efficiency is measured as a function of p_T and η of a lepton. From the study, we assume that the reconstruction efficiency for an electron is unity with uncertainty at the level of 1.5 %.

	$0 < \eta < 0.8$	$0.8 < \eta < 1.2$	$1.2 < \eta < 2.4$
N-1 Efficiencies in data			
$10 < p_T < 15$	0.9650 ± 0.0023	0.9576 ± 0.0023	0.9352 ± 0.0014
$15 < p_T < 20$	0.9652 ± 0.0005	0.9500 ± 0.0016	0.9389 ± 0.0008
$20 < p_T < 30$	0.9687 ± 0.0004	0.9565 ± 0.0006	0.9497 ± 0.0011
$30 < p_T < 40$	0.9720 ± 0.0002	0.9611 ± 0.0006	0.9536 ± 0.0025
$40 < p_T < 50$	0.9732 ± 0.0001	0.9640 ± 0.0004	0.9599 ± 0.0005
$50 < p_T < 7000$	0.9675 ± 0.0004	0.9546 ± 0.0006	0.9331 ± 0.0003
N-1 Efficiencies in simulation			
$10 < p_T < 15$	0.9774 ± 0.0015	0.9750 ± 0.0020	0.9537 ± 0.0015
$15 < p_T < 20$	0.9808 ± 0.0008	0.9738 ± 0.0013	0.9580 ± 0.0010
$20 < p_T < 30$	0.9828 ± 0.0003	0.9739 ± 0.0005	0.9624 ± 0.0004
$30 < p_T < 40$	0.9844 ± 0.0001	0.9766 ± 0.0003	0.9659 ± 0.0002
$40 < p_T < 50$	0.9849 ± 0.0001	0.9778 ± 0.0002	0.9696 ± 0.0002
$50 < p_T < 7000$	0.9819 ± 0.0002	0.9715 ± 0.0004	0.9493 ± 0.0004
Simulation-to-data scale factors			
$10 < p_T < 15$	0.9872 ± 0.0028	0.9821 ± 0.0031	0.9806 ± 0.0021
$15 < p_T < 20$	0.9841 ± 0.0009	0.9755 ± 0.0021	0.9801 ± 0.0013
$20 < p_T < 30$	0.9857 ± 0.0005	0.9821 ± 0.0008	0.9868 ± 0.0012
$30 < p_T < 40$	0.9874 ± 0.0002	0.9841 ± 0.0007	0.9873 ± 0.0026
$40 < p_T < 50$	0.9881 ± 0.0002	0.9859 ± 0.0004	0.9899 ± 0.0005
$50 < p_T < 7000$	0.9854 ± 0.0005	0.9826 ± 0.0008	0.9829 ± 0.0005

Table 4.4: HWW Muon V00-02-09 Moriond jae NM1Eff ID

Table 4.4 and 4.5 show muon N-1 efficiencies in data and simulation, and data-to-simulation scale factors for ID and ISO selections, respectively. The scale factors are close to unity in all bins.

	$0 < \eta < 0.8$	$0.8 < \eta < 1.2$	$1.2 < \eta < 2.4$
N-1 Efficiencies in data			
$10 < p_T < 15$	0.6693 ± 0.0037	0.6776 ± 0.0040	0.7590 ± 0.0017
$15 < p_T < 20$	0.7447 ± 0.0021	0.7615 ± 0.0030	0.8347 ± 0.0000
$20 < p_T < 30$	0.8903 ± 0.0008	0.8932 ± 0.0006	0.9044 ± 0.0006
$30 < p_T < 40$	0.9606 ± 0.0007	0.9636 ± 0.0007	0.9659 ± 0.0002
$40 < p_T < 50$	0.9837 ± 0.0001	0.9855 ± 0.0000	0.9886 ± 0.0001
$50 < p_T < 7000$	0.9875 ± 0.0002	0.9879 ± 0.0002	0.9910 ± 0.0002
N-1 Efficiencies in simulation			
$10 < p_T < 15$	0.6556 ± 0.0037	0.6832 ± 0.0048	0.7322 ± 0.0027
$15 < p_T < 20$	0.7519 ± 0.0020	0.7691 ± 0.0030	0.8139 ± 0.0017
$20 < p_T < 30$	0.8954 ± 0.0006	0.8962 ± 0.0009	0.8847 ± 0.0006
$30 < p_T < 40$	0.9642 ± 0.0002	0.9664 ± 0.0003	0.9584 ± 0.0002
$40 < p_T < 50$	0.9857 ± 0.0001	0.9878 ± 0.0002	0.9872 ± 0.0001
$50 < p_T < 7000$	0.9885 ± 0.0002	0.9902 ± 0.0003	0.9899 ± 0.0002
Simulation-to-data scale factors			
$10 < p_T < 15$	1.0209 ± 0.0081	0.9917 ± 0.0092	1.0365 ± 0.0044
$15 < p_T < 20$	0.9904 ± 0.0038	0.9901 ± 0.0055	1.0256 ± 0.0021
$20 < p_T < 30$	0.9944 ± 0.0011	0.9966 ± 0.0012	1.0222 ± 0.0010
$30 < p_T < 40$	0.9962 ± 0.0007	0.9971 ± 0.0008	1.0078 ± 0.0003
$40 < p_T < 50$	0.9980 ± 0.0001	0.9977 ± 0.0002	1.0014 ± 0.0002
$50 < p_T < 7000$	0.9990 ± 0.0003	0.9977 ± 0.0003	1.0011 ± 0.0002

Table 4.5: HWW Muon V00-02-09 Moriond jae NM1Eff Iso

In case of muon, the systematic uncertainty due to N-1 method is negligible(< 0.2 %) compared to reconstruction efficiency which is at the level of 1.5 %.

4.1.3 Trigger Efficiency

!! FIX CAPTION of the tables !!

Tow things to completley understand: (1) randomization of probe leg (2) formula for per event trg eff. =, got it, but the formula in AN2012-386 does not seem right, especially the dZ part. Maybe just mention that inefficiency due to dZ is very low and ignored in the actual calculation. This is the actual calculation :

```

evt_eff =
1 - ( (1-eff_dbl_1_leadingleg)*(1-eff_dbl_2_leadingleg) +
      eff_dbl_1_leadingleg*(1-eff_dbl_2_trailingleg) +
      eff_dbl_2_leadingleg*(1-eff_dbl_1_trailingleg))
+ eff_sgl_2*(1-eff_dbl_1_trailingleg)
+ eff_sgl_1*(1-eff_dbl_2_trailingleg)

```

The analysis uses a combination of single-lepton and double-lepton triggers. For double-lepton trigger there is a requirement on dZ, the longitudinal distance between two lepton vertices, on top of the requirement on each leg. This requirement is imposed to select events from hard interactions not from pileup events. Only are events that pass both requirements recorded in the data sample under study. Thus, there is 100 % correlation between the two leptons, *i.e.* if one lepton passed the per lepton requirement, the other lepton passed it as well, otherwise trigger objects have not been stored at all in the data samples under study. This introduces a slight change in the Tag-And-Probe method that only is one tag selected in an event and we do it by selecting a tag randomly.

The dZ requirement for the double-lepton triggers is designed to be highly efficient. However, in the early part of data in 2012 there was a technical issue that caused inefficiency of dZ requirement for double-muon triggers at the level of 15 %. The inefficiency is absorbed by using single-lepton triggers to a negligible level. Thus, in the per event trigger efficiency calculation we assume dZ efficiency is 100 %.

The efficiency of each leg of double-lepton triggers is measured separately because there are different requirements imposed to them. For $e\mu$ triggers, we assume that the efficiency of both legs can be modelled by measurements of per leg efficiency of double-electron and double-muon triggers.[\[ref?\]](#) This assumption was validated by measuring $e\mu$ trigger efficiency using $t\bar{t}$ events with $\text{MET} > 20$ GeV. In order to avoid possible bias the muon leg efficiency was measured using events passing single-electron trigger and the electron leg efficiency was measured using events passing single-muon trigger. The result turned out to be consistent with our model using per leg efficiency from measurements of double-lepton trigger within the statistical uncertainties.

Given the per leg efficiencies of double-lepton triggers and single-lepton trigger efficiency, the per event trigger efficiency is calculated. The requirement of the single-lepton trigger is tighter than the requirements applied to each leg in double-lepton trigger. So, there are only three cases that an event passes trigger requirements.

1. Both leptons pass the requirement on each leg in double-lepton trigger and dZ
2. Both leptons pass the requirement on each leg in double-lepton trigger, but failed dZ. At least one of the leptons pass single-lepton trigger
3. One of the leptons fail double-lepton trigger requirements, but the other lepton passes single-lepton trigger

As mentioned above, dZ efficiency is assumed to be 100 % in our calculation, so (2) is not included in the per event efficiency calculation. Figure 4.1 shows the failing cases of double-lepton trigger. There are three online cases for each lepton, which are passing leading leg requirement(L), passing trailing lepton requirement(T), and passing none of them(F). Shaded boxes show that each lepton falls into that category of offline requirement. There are $9(3 \times 3)$ possible combinations in total, of which there are 6 cases that the trigger fails. Category 1(4 combinations) is the case where none of the two leptons pass leading leg requirement. Category 2 and

category 1		category 2		category 3	
Lepton 1	Lepton 2	Lepton 1	Lepton 2	Lepton 1	Lepton 2
L	L	L	L	L	L
!L && T	!L && T	!L && T	!L && T	!L && T	!L && T
F	F	F	F	F	F

Figure 4.1: Diagrams for the cases where double-lepton triggers fail. Lepton1(2) denotes offline leptons. L means leading leg requirement of double-lepton trigger. T means trailing leg requirement of double-lepton trigger. F means failing of trailing lepton requirement, thus leading lepton requirement, of double-lepton trigger. Shade means that the corresponding offline lepton falls into that online requirement.

3 are the cases where one lepton passes leading leg requirement but the other leg fails trailing leg requirement. Converting this into equations, we have

$$\epsilon_{double-lepton}(p_{T1}, \eta_1, p_{T2}, \eta_2) = 1 - \left[\right. \quad (4.3)$$

$$\underbrace{(1 - \epsilon_{DL}(p_{T1}, \eta_1))(1 - \epsilon_{DL}(p_{T2}, \eta_2))}_{\text{category 1}} \quad (4.4)$$

$$+ \underbrace{\epsilon_{DL}(p_{T2}, \eta_2)(1 - \epsilon_{DT}(p_{T1}, \eta_1))}_{\text{category 2}} \quad (4.5)$$

$$+ \underbrace{\epsilon_{DL}(p_{T1}, \eta_1)(1 - \epsilon_{DT}(p_{T2}, \eta_2))}_{\text{category 3}} \left. \right] \quad (4.6)$$

where $p_{T1(2)}$ and $\eta_{1(2)}$ are p_T and η of offline leptons, ϵ_{DL} is the efficiency for the leading leg of double-lepton trigger, and ϵ_{DT} is the efficiency for the trailing leg of double-lepton trigger. Each term corresponds to the 3 categories in Figure 4.1.

In case the double-lepton trigger fails because one of the legs fails, the other leg which passed double-lepton trigger requirement might pass single lepton trigger. This way, inefficiency of double-lepton trigger can be recovered by single-lepton trigger. The recovery of efficiency by single-lepton trigger is

$$\epsilon_{single-lepton}(p_{T1}, \eta_1, p_{T2}, \eta_2) = \underbrace{(1 - \epsilon_{DT}(p_{T1}, \eta_1)) \epsilon_S(p_{T2}, \eta_2)}_{\text{category 4}} \quad (4.7)$$

$$+ \underbrace{(1 - \epsilon_{DT}(p_{T2}, \eta_2)) \epsilon_S(p_{T1}, \eta_1)}_{\text{category 5}} \quad (4.8)$$

where ϵ_S is the efficiency of single-lepton trigger. Therefore, the total per-event trigger efficiency is given by

$$\epsilon_{event}(p_{T1}, \eta_1, p_{T2}, \eta_2) = 1 - \left[(1 - \epsilon_{DL}(p_{T1}, \eta_1)) (1 - \epsilon_{DL}(p_{T2}, \eta_2)) \right. \quad (4.9)$$

$$\left. + \epsilon_{DL}(p_{T2}, \eta_2) (1 - \epsilon_{DT}(p_{T1}, \eta_1)) \right. \quad (4.10)$$

$$\left. + \epsilon_{DL}(p_{T1}, \eta_1) (1 - \epsilon_{DT}(p_{T2}, \eta_2)) \right] \quad (4.11)$$

$$+ (1 - \epsilon_{DT}(p_{T1}, \eta_1)) \epsilon_S(p_{T2}, \eta_2) \quad (4.12)$$

$$+ (1 - \epsilon_{DT}(p_{T2}, \eta_2)) \epsilon_S(p_{T1}, \eta_1) \quad (4.13)$$

	$0 < \eta < 0.8$	$0.8 < \eta < 1.479$	$1.479 < \eta < 2$	$2 < \eta < 2.5$
$10 < p_T < 12.5$	1.0000 ± 0.0045	0.9946 ± 0.0043	0.9853 ± 0.0191	0.9724 ± 0.0213
$12.5 < p_T < 15$	1.0000 ± 0.0011	0.9934 ± 0.0024	1.0000 ± 0.0036	0.9773 ± 0.0095
$15 < p_T < 17.5$	0.9982 ± 0.0010	0.9971 ± 0.0011	0.9949 ± 0.0030	0.9886 ± 0.0048
$17.5 < p_T < 20$	0.9990 ± 0.0005	0.9969 ± 0.0008	0.9952 ± 0.0020	0.9884 ± 0.0034
$20 < p_T < 22.5$	0.9993 ± 0.0004	0.9980 ± 0.0006	0.9970 ± 0.0012	0.9873 ± 0.0024
$22.5 < p_T < 25$	0.9997 ± 0.0002	0.9980 ± 0.0004	0.9962 ± 0.0010	0.9911 ± 0.0016
$25 < p_T < 27.5$	0.9994 ± 0.0002	0.9982 ± 0.0003	0.9965 ± 0.0007	0.9905 ± 0.0013
$27.5 < p_T < 30$	0.9993 ± 0.0001	0.9985 ± 0.0002	0.9975 ± 0.0005	0.9908 ± 0.0011
$30 < p_T < 35$	0.9995 ± 0.0001	0.9986 ± 0.0001	0.9972 ± 0.0003	0.9920 ± 0.0005
$35 < p_T < 40$	0.9996 ± 0.0000	0.9987 ± 0.0001	0.9972 ± 0.0002	0.9921 ± 0.0004
$40 < p_T < 50$	0.9997 ± 0.0000	0.9990 ± 0.0000	0.9973 ± 0.0001	0.9925 ± 0.0003
$50 < p_T < 7000$	0.9997 ± 0.0000	0.9992 ± 0.0001	0.9978 ± 0.0002	0.9922 ± 0.0005

Table 4.6: HWW Electron V00-02-09 Moriond jae NM1Eff TrigDzDbl

The efficiency of dZ, leading and trailing leg requirements for double-electron triggers is shown in Table 4.6 - 4.8. The efficiency of single-electron trigger is shown in 4.9.

	$0 < \eta < 0.8$	$0.8 < \eta < 1.479$	$1.479 < \eta < 2$	$2 < \eta < 2.5$
$10 < p_T < 12.5$	0.0000 ± 0.0041	0.0000 ± 0.0021	0.0000 ± 0.0102	0.0000 ± 0.0112
$12.5 < p_T < 15$	0.0000 ± 0.0011	0.0000 ± 0.0009	0.0092 ± 0.0062	0.0021 ± 0.0049
$15 < p_T < 17.5$	0.0437 ± 0.0035	0.0460 ± 0.0034	0.2456 ± 0.0128	0.2300 ± 0.0148
$17.5 < p_T < 20$	0.8312 ± 0.0044	0.6617 ± 0.0057	0.8570 ± 0.0080	0.8365 ± 0.0098
$20 < p_T < 22.5$	0.9618 ± 0.0019	0.9560 ± 0.0021	0.9768 ± 0.0027	0.9685 ± 0.0035
$22.5 < p_T < 25$	0.9709 ± 0.0013	0.9721 ± 0.0014	0.9843 ± 0.0018	0.9785 ± 0.0024
$25 < p_T < 27.5$	0.9784 ± 0.0009	0.9764 ± 0.0010	0.9879 ± 0.0013	0.9859 ± 0.0016
$27.5 < p_T < 30$	0.9823 ± 0.0006	0.9809 ± 0.0008	0.9884 ± 0.0010	0.9869 ± 0.0012
$30 < p_T < 35$	0.9849 ± 0.0003	0.9842 ± 0.0004	0.9901 ± 0.0005	0.9869 ± 0.0006
$35 < p_T < 40$	0.9880 ± 0.0002	0.9863 ± 0.0003	0.9925 ± 0.0003	0.9907 ± 0.0004
$40 < p_T < 50$	0.9900 ± 0.0001	0.9903 ± 0.0001	0.9945 ± 0.0002	0.9912 ± 0.0003
$50 < p_T < 7000$	0.9910 ± 0.0002	0.9925 ± 0.0002	0.9958 ± 0.0003	0.9911 ± 0.0005

Table 4.7: HWW Electron V00-02-09 Moriond jae NM1Eff TrigLeadDbl

	$0 < \eta < 0.8$	$0.8 < \eta < 1.479$	$1.479 < \eta < 2$	$2 < \eta < 2.5$
$10 < p_T < 12.5$	0.9101 ± 0.0157	0.8313 ± 0.0135	0.7598 ± 0.0362	0.8841 ± 0.0306
$12.5 < p_T < 15$	0.9633 ± 0.0051	0.9284 ± 0.0060	0.9316 ± 0.0126	0.9382 ± 0.0132
$15 < p_T < 17.5$	0.9685 ± 0.0030	0.9554 ± 0.0034	0.9572 ± 0.0066	0.9595 ± 0.0076
$17.5 < p_T < 20$	0.9673 ± 0.0022	0.9665 ± 0.0023	0.9716 ± 0.0041	0.9774 ± 0.0044
$20 < p_T < 22.5$	0.9695 ± 0.0017	0.9699 ± 0.0018	0.9762 ± 0.0028	0.9786 ± 0.0030
$22.5 < p_T < 25$	0.9731 ± 0.0012	0.9745 ± 0.0013	0.9764 ± 0.0021	0.9758 ± 0.0025
$25 < p_T < 27.5$	0.9771 ± 0.0009	0.9779 ± 0.0010	0.9831 ± 0.0015	0.9831 ± 0.0017
$27.5 < p_T < 30$	0.9810 ± 0.0007	0.9807 ± 0.0008	0.9829 ± 0.0012	0.9842 ± 0.0013
$30 < p_T < 35$	0.9828 ± 0.0003	0.9831 ± 0.0004	0.9830 ± 0.0006	0.9840 ± 0.0007
$35 < p_T < 40$	0.9850 ± 0.0002	0.9843 ± 0.0003	0.9861 ± 0.0004	0.9879 ± 0.0005
$40 < p_T < 50$	0.9870 ± 0.0001	0.9874 ± 0.0002	0.9883 ± 0.0002	0.9885 ± 0.0003
$50 < p_T < 7000$	0.9882 ± 0.0003	0.9893 ± 0.0003	0.9900 ± 0.0004	0.9888 ± 0.0006

Table 4.8: HWW Electron V00-02-09 Moriond jae NM1Eff TrigTrailDbl

	$0 < \eta < 0.8$	$0.8 < \eta < 1.479$	$1.479 < \eta < 2$	$2 < \eta < 2.5$
$10 < p_T < 12.5$	0.0000 ± 0.0021	0.0000 ± 0.0010	0.0000 ± 0.0051	0.0000 ± 0.0057
$12.5 < p_T < 15$	0.0000 ± 0.0005	0.0000 ± 0.0004	0.0000 ± 0.0017	0.0000 ± 0.0020
$15 < p_T < 17.5$	0.0000 ± 0.0002	0.0000 ± 0.0002	0.0000 ± 0.0008	0.0000 ± 0.0010
$17.5 < p_T < 20$	0.0000 ± 0.0001	0.0000 ± 0.0001	0.0002 ± 0.0005	0.0000 ± 0.0006
$20 < p_T < 22.5$	0.0000 ± 0.0001	0.0000 ± 0.0001	0.0005 ± 0.0004	0.0007 ± 0.0005
$22.5 < p_T < 25$	0.0006 ± 0.0002	0.0006 ± 0.0002	0.0118 ± 0.0011	0.0250 ± 0.0018
$25 < p_T < 27.5$	0.0255 ± 0.0007	0.0251 ± 0.0007	0.1320 ± 0.0026	0.1636 ± 0.0032
$27.5 < p_T < 30$	0.6009 ± 0.0016	0.4072 ± 0.0018	0.4926 ± 0.0031	0.4710 ± 0.0035
$30 < p_T < 35$	0.8905 ± 0.0005	0.8634 ± 0.0007	0.6775 ± 0.0015	0.6602 ± 0.0018
$35 < p_T < 40$	0.9171 ± 0.0004	0.9012 ± 0.0004	0.7285 ± 0.0011	0.7103 ± 0.0013
$40 < p_T < 50$	0.9361 ± 0.0002	0.9239 ± 0.0003	0.7618 ± 0.0007	0.7298 ± 0.0009
$50 < p_T < 7000$	0.9471 ± 0.0004	0.9402 ± 0.0005	0.7808 ± 0.0012	0.7374 ± 0.0017

Table 4.9: HWW Electron V00-02-09 Moriond jae NM1Eff TrigSgl

	$0 < \eta < 0.8$	$0.8 < \eta < 1.2$	$1.2 < \eta < 2.1$	$2.1 < \eta < 2.4$
$10 < p_T < 12.5$	0.9710 ± 0.0045	0.9687 ± 0.0045	0.9572 ± 0.0029	0.9682 ± 0.0044
$12.5 < p_T < 15$	0.9714 ± 0.0028	0.9692 ± 0.0032	0.9612 ± 0.0022	0.9617 ± 0.0040
$15 < p_T < 17.5$	0.9794 ± 0.0017	0.9702 ± 0.0026	0.9710 ± 0.0016	0.9688 ± 0.0031
$17.5 < p_T < 20$	0.9907 ± 0.0009	0.9838 ± 0.0016	0.9819 ± 0.0011	0.9764 ± 0.0023
$20 < p_T < 22.5$	0.9912 ± 0.0007	0.9862 ± 0.0012	0.9823 ± 0.0009	0.9755 ± 0.0020
$22.5 < p_T < 25$	0.9896 ± 0.0006	0.9873 ± 0.0009	0.9828 ± 0.0007	0.9785 ± 0.0016
$25 < p_T < 27.5$	0.9897 ± 0.0005	0.9886 ± 0.0007	0.9815 ± 0.0006	0.9784 ± 0.0014
$27.5 < p_T < 30$	0.9900 ± 0.0004	0.9874 ± 0.0006	0.9813 ± 0.0005	0.9794 ± 0.0011
$30 < p_T < 35$	0.9911 ± 0.0002	0.9869 ± 0.0004	0.9810 ± 0.0003	0.9805 ± 0.0006
$35 < p_T < 40$	0.9918 ± 0.0001	0.9862 ± 0.0003	0.9790 ± 0.0003	0.9789 ± 0.0006
$40 < p_T < 50$	0.9934 ± 0.0001	0.9855 ± 0.0002	0.9767 ± 0.0002	0.9777 ± 0.0004
$50 < p_T < 7000$	0.9937 ± 0.0002	0.9855 ± 0.0003	0.9747 ± 0.0004	0.9799 ± 0.0009

Table 4.10: HWW Muon V00-02-09 Moriond jae NM1Eff TrigDzDbI

	$0 < \eta < 0.8$	$0.8 < \eta < 1.2$	$1.2 < \eta < 2.1$	$2.1 < \eta < 2.4$
$10 < p_T < 12.5$	0.0005 ± 0.0012	0.0114 ± 0.0030	0.0034 ± 0.0010	0.0085 ± 0.0025
$12.5 < p_T < 15$	0.0005 ± 0.0006	0.0188 ± 0.0026	0.0068 ± 0.0010	0.0092 ± 0.0021
$15 < p_T < 17.5$	0.2500 ± 0.0049	0.2363 ± 0.0060	0.2688 ± 0.0040	0.2442 ± 0.0069
$17.5 < p_T < 20$	0.9696 ± 0.0015	0.9169 ± 0.0033	0.9036 ± 0.0023	0.8007 ± 0.0055
$20 < p_T < 22.5$	0.9714 ± 0.0011	0.9243 ± 0.0026	0.9138 ± 0.0018	0.8176 ± 0.0046
$22.5 < p_T < 25$	0.9717 ± 0.0009	0.9269 ± 0.0021	0.9236 ± 0.0015	0.8479 ± 0.0037
$25 < p_T < 27.5$	0.9717 ± 0.0007	0.9311 ± 0.0017	0.9221 ± 0.0012	0.8506 ± 0.0031
$27.5 < p_T < 30$	0.9712 ± 0.0006	0.9280 ± 0.0014	0.9233 ± 0.0010	0.8558 ± 0.0026
$30 < p_T < 35$	0.9706 ± 0.0003	0.9289 ± 0.0008	0.9198 ± 0.0006	0.8692 ± 0.0014
$35 < p_T < 40$	0.9722 ± 0.0002	0.9286 ± 0.0006	0.9206 ± 0.0005	0.8796 ± 0.0012
$40 < p_T < 50$	0.9726 ± 0.0002	0.9320 ± 0.0004	0.9215 ± 0.0003	0.8889 ± 0.0009
$50 < p_T < 7000$	0.9725 ± 0.0003	0.9337 ± 0.0007	0.9216 ± 0.0006	0.9016 ± 0.0018

Table 4.11: HWW Muon V00-02-09 Moriond jae NM1Eff TrigLeadDbl

	$0 < \eta < 0.8$	$0.8 < \eta < 1.2$	$1.2 < \eta < 2.1$	$2.1 < \eta < 2.4$
$10 < p_T < 12.5$	0.0000 ± 0.0005	0.0000 ± 0.0005	0.0001 ± 0.0002	0.0000 ± 0.0004
$12.5 < p_T < 15$	0.0000 ± 0.0002	0.0001 ± 0.0003	0.0002 ± 0.0002	0.0000 ± 0.0003
$15 < p_T < 17.5$	0.0000 ± 0.0001	0.0004 ± 0.0003	0.0001 ± 0.0001	0.0000 ± 0.0002
$17.5 < p_T < 20$	0.0000 ± 0.0001	0.0015 ± 0.0004	0.0004 ± 0.0001	0.0000 ± 0.0002
$20 < p_T < 22.5$	0.0004 ± 0.0001	0.0030 ± 0.0004	0.0028 ± 0.0003	0.0000 ± 0.0001
$22.5 < p_T < 25$	0.4031 ± 0.0018	0.3699 ± 0.0027	0.3912 ± 0.0019	0.0000 ± 0.0001
$25 < p_T < 27.5$	0.8847 ± 0.0010	0.8076 ± 0.0018	0.7733 ± 0.0014	0.0001 ± 0.0001
$27.5 < p_T < 30$	0.8955 ± 0.0008	0.8172 ± 0.0015	0.7881 ± 0.0011	0.0002 ± 0.0001
$30 < p_T < 35$	0.9100 ± 0.0004	0.8267 ± 0.0008	0.7968 ± 0.0006	0.0001 ± 0.0000
$35 < p_T < 40$	0.9230 ± 0.0003	0.8368 ± 0.0006	0.8048 ± 0.0005	0.0001 ± 0.0000
$40 < p_T < 50$	0.9350 ± 0.0002	0.8480 ± 0.0004	0.8161 ± 0.0003	0.0001 ± 0.0000
$50 < p_T < 7000$	0.9408 ± 0.0003	0.8526 ± 0.0007	0.8207 ± 0.0006	0.0002 ± 0.0001

Table 4.12: HWW Muon V00-02-09 Moriond jae NM1Eff TrigSgl

	$0 < \eta < 0.8$	$0.8 < \eta < 1.2$	$1.2 < \eta < 2.1$	$2.1 < \eta < 2.4$
$10 < p_T < 12.5$	0.9838 ± 0.0035	0.9752 ± 0.0041	0.9779 ± 0.0021	0.9371 ± 0.0057
$12.5 < p_T < 15$	0.9850 ± 0.0021	0.9735 ± 0.0030	0.9814 ± 0.0016	0.9403 ± 0.0047
$15 < p_T < 17.5$	0.9846 ± 0.0015	0.9770 ± 0.0023	0.9817 ± 0.0013	0.9391 ± 0.0040
$17.5 < p_T < 20$	0.9824 ± 0.0012	0.9772 ± 0.0018	0.9807 ± 0.0011	0.9422 ± 0.0033
$20 < p_T < 22.5$	0.9831 ± 0.0009	0.9791 ± 0.0014	0.9812 ± 0.0009	0.9388 ± 0.0029
$22.5 < p_T < 25$	0.9824 ± 0.0007	0.9782 ± 0.0012	0.9826 ± 0.0007	0.9468 ± 0.0024
$25 < p_T < 27.5$	0.9837 ± 0.0006	0.9797 ± 0.0010	0.9822 ± 0.0006	0.9438 ± 0.0020
$27.5 < p_T < 30$	0.9831 ± 0.0005	0.9792 ± 0.0008	0.9829 ± 0.0005	0.9440 ± 0.0017
$30 < p_T < 35$	0.9827 ± 0.0002	0.9797 ± 0.0004	0.9814 ± 0.0003	0.9482 ± 0.0010
$35 < p_T < 40$	0.9840 ± 0.0002	0.9792 ± 0.0003	0.9825 ± 0.0002	0.9501 ± 0.0008
$40 < p_T < 50$	0.9846 ± 0.0001	0.9800 ± 0.0002	0.9831 ± 0.0002	0.9551 ± 0.0006
$50 < p_T < 7000$	0.9851 ± 0.0002	0.9804 ± 0.0004	0.9829 ± 0.0003	0.9563 ± 0.0013

Table 4.13: HWW Muon V00-02-09 Moriond jae NM1Eff TrigTrailDbl

The efficiency of dZ, leading and trailing leg requirements for double-muon triggers is shown in Table 4.10 - 4.13. The efficiency of single-muon trigger is shown in 4.12.

4.2 Jet Counting Efficiency

The analysis is optimized for different categories of number of jets. But, jet counting efficiency which is defined as $\epsilon_{0/1} = \frac{N_{njet=0/1}}{N_{njet \geq 0}}$ can be different in simulation and data. So, we correct the efficiency of $H \rightarrow W^+W^- \rightarrow 2l2\nu$ in MC by a data-to-MC scale factor measured in MC and data using $Z/\gamma^* \rightarrow \ell\ell$ events. The jet counting efficiency of $H \rightarrow W^+W^- \rightarrow 2l2\nu$ events, $\epsilon_{H \rightarrow W^+W^- \rightarrow 2l2\nu}$, is calculated by

$$\epsilon_{H \rightarrow W^+W^- \rightarrow 2l2\nu} = \epsilon_{H \rightarrow W^+W^- \rightarrow 2l2\nu}^{MC} \times \frac{\epsilon_{Z/\gamma^* \rightarrow \ell\ell}^{Data}}{\epsilon_{Z/\gamma^* \rightarrow \ell\ell}^{MC}} \quad (4.14)$$

where $\epsilon_{H \rightarrow W^+W^- \rightarrow 2l2\nu}^{MC}$ is jet counting efficiency of $H \rightarrow W^+W^- \rightarrow 2l2\nu$ in simulation, and $\frac{\epsilon_{Z/\gamma^* \rightarrow \ell\ell}^{Data}}{\epsilon_{Z/\gamma^* \rightarrow \ell\ell}^{MC}}$ is a data-to-simulation scale factor measured using $Z/\gamma^* \rightarrow \ell\ell$ events. The efficiencies of $Z/\gamma^* \rightarrow \ell\ell$ events are evaluated using Drell-Yan events with dilepton mass within 7.5 GeV of the Z peak.

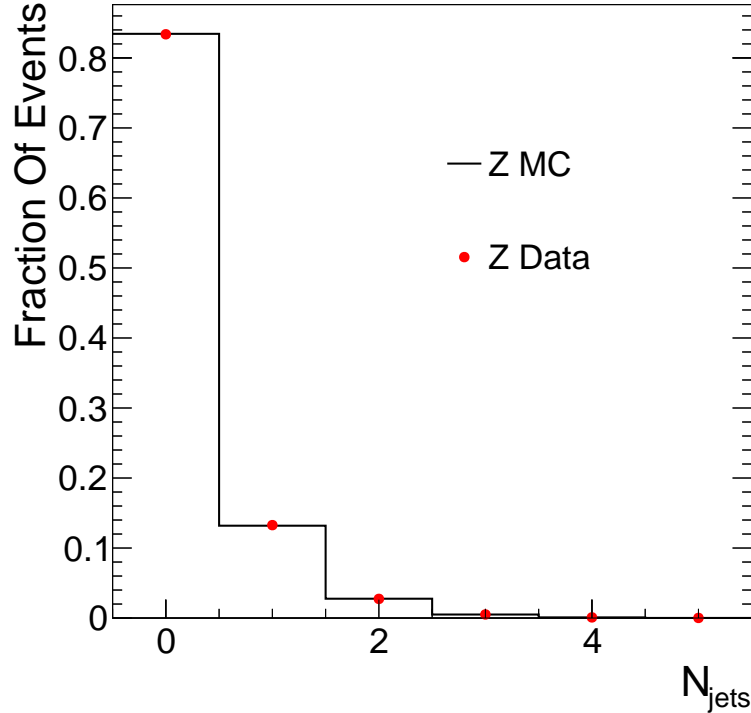


Figure 4.2: The number of Jets observed in data (red solid dot) and MC (black line) for the Z events.

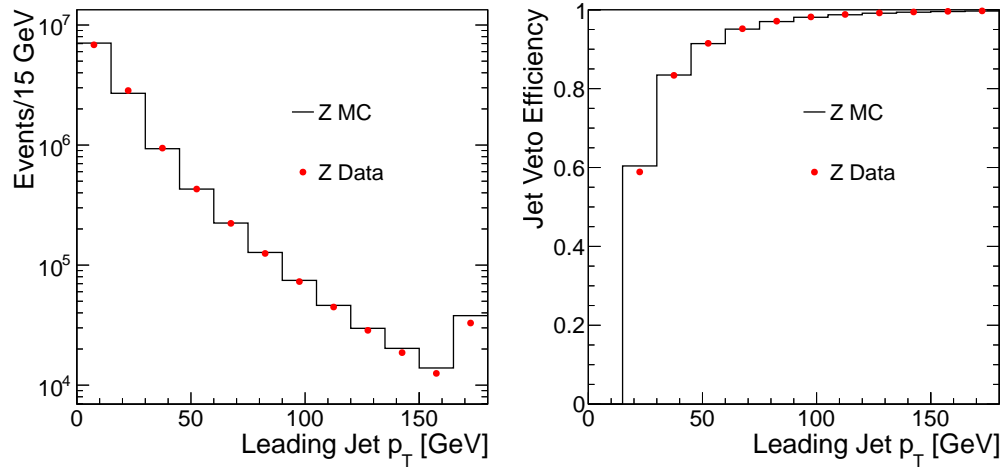


Figure 4.3: The leading jet p_T ?? and the jet veto efficiency as a function of the leading jet p_T ?? in data (red solid dot) and MC (black line) for the Z events.

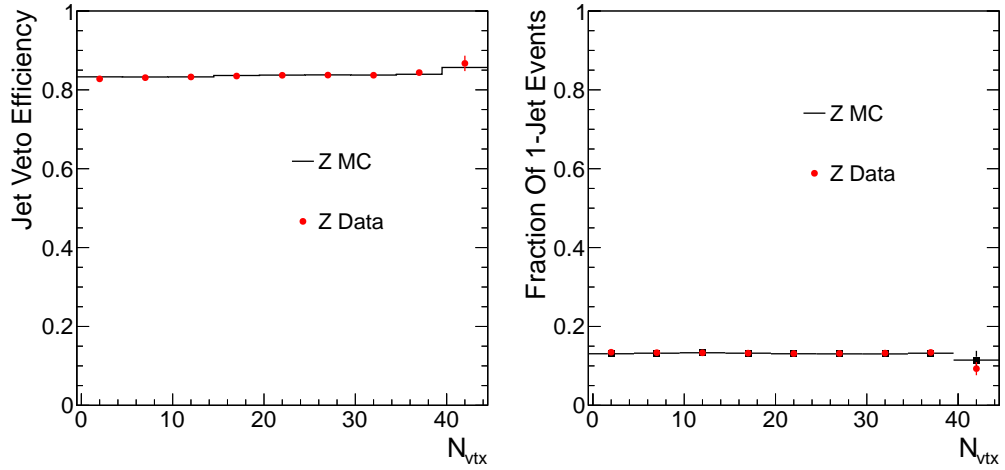


Figure 4.4: The fraction of events with 0 Jet ?? and 1 Jet ?? as a function of the number of vertices, comparing data (red solid dot) and MC (black solid square) for the Z events.

Figure 4.2 shows distribution of number of jets for data and MC. In all bins good agreement with difference less than 1% is shown. The systematic uncertainty to jet counting efficiency comes from statistics when measuring data-to-MC scale factor and theoretical uncertainty of jet counting in $H \rightarrow W^+W^- \rightarrow 2l2\nu$ simulation. The former is less than 1% being negligible compared to theoretical uncertainty which is at the level of 15%. This uncertainty will be discussed in the chapter for Systematic Uncertainty 7.

Figure 4.3 shows p_T distribution of leading jet (left) and jet veto efficiency as a function of leading jet p_T (right) With the jet p_T threshold 30 GeV, agreement between data and MC is very good. Figure 4.4 shows fraction of events with 0 jet and 1 jet as a function of number of reconstructed vertexes(Nvtx). Data and MC show very good agreement. Dependence of efficiencies on Nvtx is small in both data and MC. Thus, with the chosen jet identification, jet counting efficiency is not affected by reweighting by number of Pile-Up events. (fix this sentence to read better)

Chapter 5

Signal Extraction

5.1 Cut-based Method

5.2 Shape-based Method

Chapter 6

Background Estimation

Overview : would be good to have a diagram that shows the connection between estimations

6.1 WW

6.2 Top

6.3 DY

6.4 W+jets

- $p_T > 10 \text{ GeV}$ and $|\eta| < 2.5$
- $\sigma_{i\eta i\eta} < 0.01/0.03$ (barrel/endcap)
- $|\Delta\phi_{in}| < 0.15/0.10$ (barrel/endcap)
- $|\Delta\eta_{in}| < 0.007/0.009$ (barrel/endcap)
- $H/E < 0.12/0.10$ (barrel/endcap)
- $\frac{\sum_{\text{tracks with dR} < 0.3} E_T}{p_T} < 0.2$
- $\frac{(\sum_{\text{ECAL with dR} < 0.3} E_T) - 1}{p_T} < 0.2$
- $\frac{\sum_{\text{HCAL with dR} < 0.3} E_T}{p_T} < 0.2$
- conversion rejection (will be discussed below)

6.5 **Wgamma(*)**

6.6 **DYtt**

6.7 **WZ/ZZ**

Chapter 7

Systematic Uncertainty

7.1 Instrumental Uncertainties

7.2 Background Estimation

7.3 Theoretical systematic uncertainties to signal

7.3.1 Jet Counting Efficiency

As discussed in chapter 4, systematic uncertainty to jet counting efficiency is dominated by $\epsilon_{H \rightarrow W^+W^- \rightarrow 2l2\nu}^{MC}$, jet counting efficiency in $H \rightarrow W^+W^- \rightarrow 2l2\nu$ simulation.

7.3.2 Acceptance

7.3.3 UEPS?

Chapter 8

Fit Validation

8.1 Validation of Fit Model

8.1.1 Fit Validation with Pseudo data

- Any intrinsic bias(sanity check) : Is there any background whose normalization is biased or constrained too much by fit?
- If one bkgd is biased, is it covered by fit?
- What are the most constrained nuisances? There are some WW-related nuisances that are constrained by a lot, so need to make sure that our fit model fits data correctly (this is a summary of this subsection, and at the same time an introduction to the next section)

8.1.2 Fit Validation with Real data

- Result on WW events : for WW
- Result on top events : for Top
- Result on SS events : for $W\gamma/W\gamma^*$ and W +jets

8.1.3 Result on qqWW events : for qqWW

In 2D analysis we rely on simulation for background shapes. The most sensitive channel, 0jet $e\mu/\mu e$, is dominated by $qq \rightarrow W^+W^-$ process. Therefore, it is important to confirm that our fit model (shape and normalization) correctly describes data. In this section, we describe a study on this subject using two control regions dominated by $qq \rightarrow W^+W^-$ process. The basic idea is that if the fit model is not correct then the prediction using one region may not be compatible with that using another region. To test this, we use post-fit result in one control region and predict the shape and normalization in another region. Following is the procedure and the result of this test.

We first select two control regions with similar statistics. It is important that both regions have similar number of events so they have similar statistical

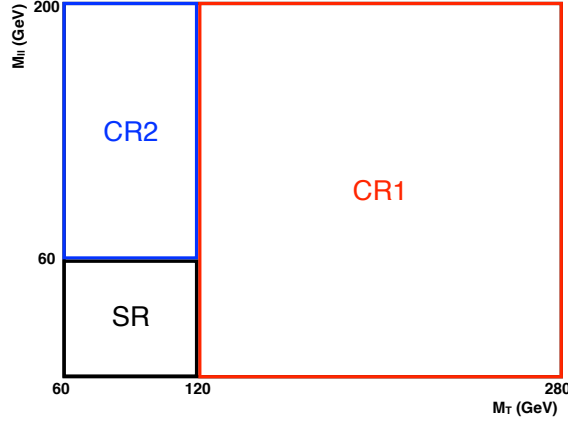


Figure 8.1: Definition of signal region(SR), and two control regions(CR1 and CR2). SR is defined by $60 < m_T < 120$ GeV and $12 < m_{\ell\ell} < 60$ GeV. CR1 is defined by $120 < m_T < 280$ GeV and $12 < m_{\ell\ell} < 200$ GeV and CR2 is defined by $60 < m_T < 120$ GeV and $60 < m_{\ell\ell} < 200$ GeV.

powers to constrain backgrounds. Figure 8.1 shows signal region(SR) which is drawn in black and two control regions, CR1 and CR2, which are drawn in red and in blue, respectively. SR is defined by $60 < m_T < 120$ GeV and $12 < m_{\ell\ell} < 60$ GeV. CR1 is defined by $120 < m_T < 280$ GeV and $12 < m_{\ell\ell} < 200$ GeV and CR2 is defined by $60 < m_T < 120$ GeV and $60 < m_{\ell\ell} < 200$ GeV. The composition of signal and backgrounds in the two control regions is summarized in Table 8.1. Both regions are dominated by $qq \rightarrow W^+W^-$ with purity of around 70(75)% in CR1(2). Signal contamination is negligible (less than 1.5%).

Region	Signal	$qq \rightarrow W^+W^-$	$gg \rightarrow W^+W^-$	WZ/ZZ	$t\bar{t}/tW$	
CR1	27.0	1321.0	113.2	46.2	289.6	
CR2	13.5	1672.7	54.5	51.5	146.1	
Full range	238.4	3969.6	210.6	132.6	498.7	
Region	$W(e\nu_e) + \text{jets}$	$W(\mu\nu_\mu) + \text{jets}$	$W\gamma$	$W\gamma^*$	$Z \rightarrow \tau\tau$	Data
CR1	54.9	22.4	6.0	19.3	2.8	1892
CR2	108.1	128.2	19.3	21.4	19.9	2155
Full range	282.8	331.8	115.6	167.8	46.0	5729

Table 8.1: Definition of signal region(SR), and two control regions(CR1 and CR2).

Because this test is only on $qq \rightarrow W^+W^-$, other processes have to be fixed in the fit. We generate new cards with all processes fixed to post-fit normalization and shape except for $qq \rightarrow W^+W^-$ process. The post-fit normalization and shapes are from a nominal fit. Hereafter, this card will be called “full range” card. In the full range card, all nuisances for $qq \rightarrow W^+W^-$ are included, but all nuisances for other processes are dropped because shape and normalization for those processes are already post-fit results. As a sanity check we compare the post-fit shape and

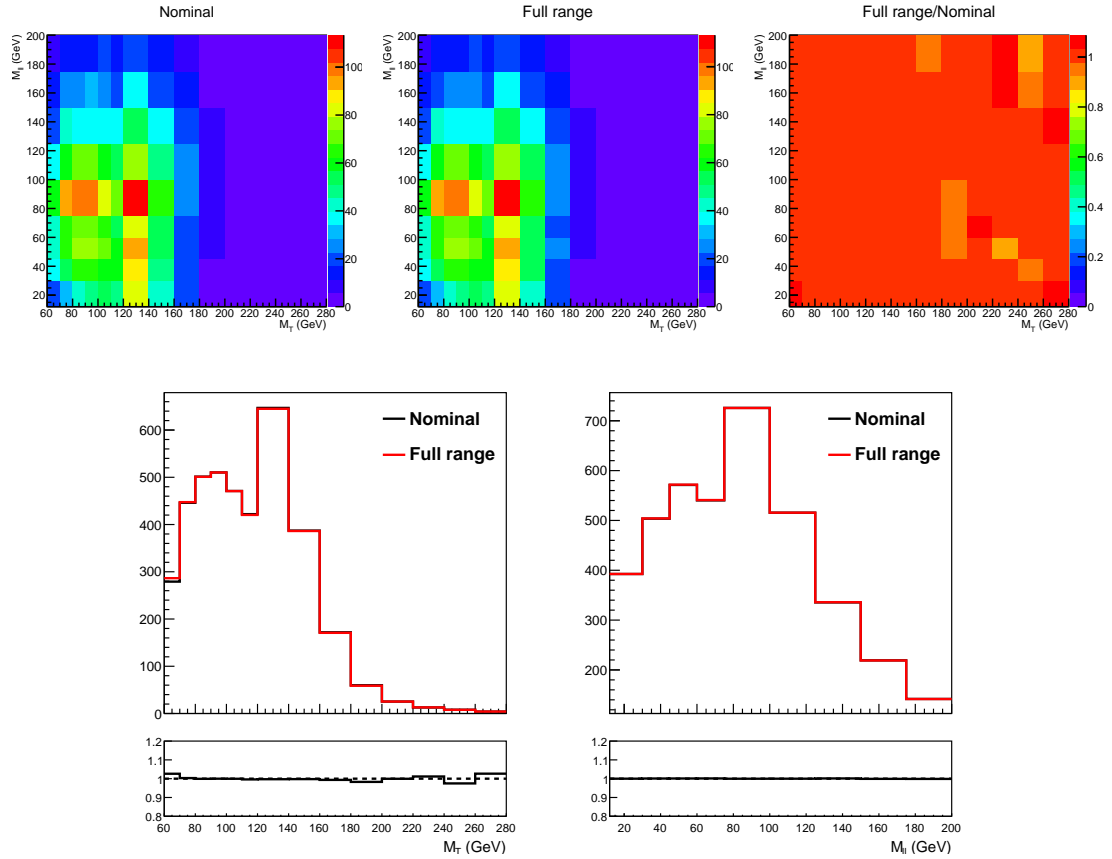


Figure 8.2: Comparison of post-fit shapes from nominal and full range fits.

normalization of $qq \rightarrow W^+W^-$ using full range card with those using the nominal card in Figure 8.2 and Table 8.2. Both shapes and normalizations using full range card are consistent with the nominal fit results.

Since the full range card has been validated, we perform two fits using only one control region. The fit using CR1(2) will be denoted as CR1(2) fit hereafter.

Fit	$qq \rightarrow VH$	$qq \rightarrow qqH$	$gg \rightarrow H$	$qq \rightarrow W^+W^-$
Nominal	4.8	1.9	144.3	3945.4
Full range	4.8	1.9	143.6	3947.0

Table 8.2: Comparison of normalization from nominal and full range fits.

In a fit using one control region, the other region is removed in the card and normalization is fixed accordingly.

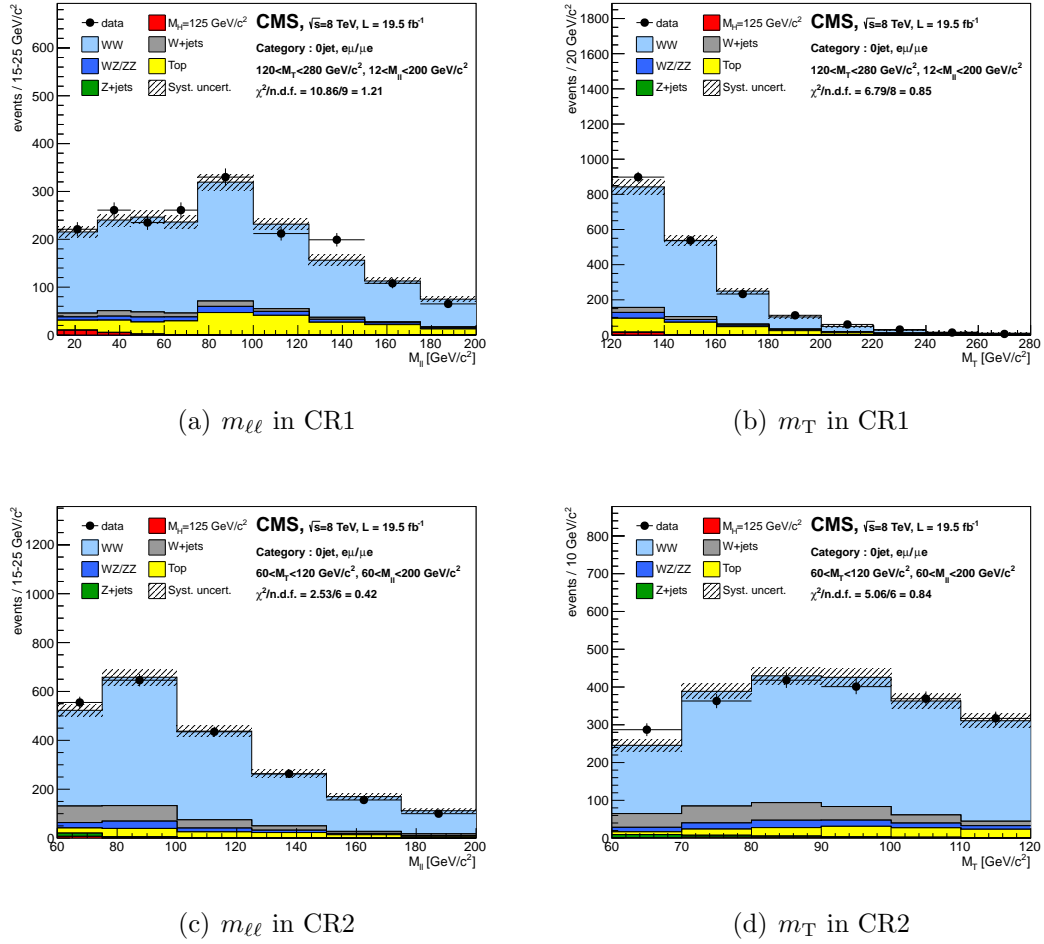


Figure 8.3: $m_{\ell\ell}$ (a,c) and m_T (b,d) distributions in CR1(top) and CR2(bottom) using the fit results of CR2 and CR1.

Figure 8.3 shows m_T and $m_{\ell\ell}$ distributions in CR1 and CR2 using normalizations from the other control regions. The uncertainty band is from pseudo-data

	full range fit	CR1 fit	CR2 fit
Best-fit μ	0.63	0.63	0.62

Table 8.3: Comparison of the best-fit μ values from nominal, full range, CR1 and CR2 fits.

sets generated using the full range card. The pseudo-data sets are generated with post-fit nuisance parameters. Variances in each bin of $qq \rightarrow W^+W^-$ and all other backgrounds are taken from full range and the nominal fits, respectively, and added in quadrature. The agreement between data and prediction is measured by $\chi^2/n.d.f.$ which is shown on each plot. All distributions show good agreement with data. This indicates that our $qq \rightarrow W^+W^-$ fit model is not biased. Table 8.3 shows the best-fit μ values from full range, CR1 and CR2 fits. Using different control regions results in consistent best-fit μ values. This is another evidence that our fit model is correct.

Therefore, we conclude that our fit model for $qq \rightarrow W^+W^-$ process fits data correctly.

8.2 Post-fit Analysis

8.2.1 Post-fit result of nuisances

In an ideal world where prediction of the central value of a nuisances is exactly what nature gives, the nuisance should not change by fit. But, in reality prediction can be wrong, thus we assign uncertainty on the nuisances. On the other hand, if the prediction is wrong by a large margin, the post-fit value of the nuisance can be far from the prediction, even larger than the uncertainty we assign. So, we need to make sure that the post-fit nuisances are within the uncertainty. A large variation of nuisances may indicate that the fit model does not describe data correctly. The measure to check this is “Pull” which is defined as

$$\text{Pull} = \frac{\theta_{\text{post-fit}} - \theta_{\text{pre-fit}}}{\sigma_{\text{pre-fit}}} \quad (8.1)$$

where $\theta_{\text{pre-fit/post-fit}}$ is the central value of a nuisance before/after fit and $\sigma_{\text{pre-fit}}$ is the assigned uncertainty to that nuisance. If the prediction is perfect and there is no variation of nuisances by fit, then the Pull should be 0. The Pull with larger than 1, *i.e.* the variation is larger than the assigned error, may indicate that the fit model is not correct.

One of the reasons why we rely on fit is that the data can constrain nuisances more than the assigned uncertainties. If there is a region that is dominated by a certain background process then the fit can use that region to constrain the background. But, if the post-fit uncertainty is larger than the assigned one, this might be an evidence that the assigned uncertainty is smaller than it is supposed to be. In order to assess any effects of this kind, we define normalized uncertainty, σ_{norm} , which is defined as a ratio of the post-fit uncertainty to pre-fit uncertainty of a nuisance,

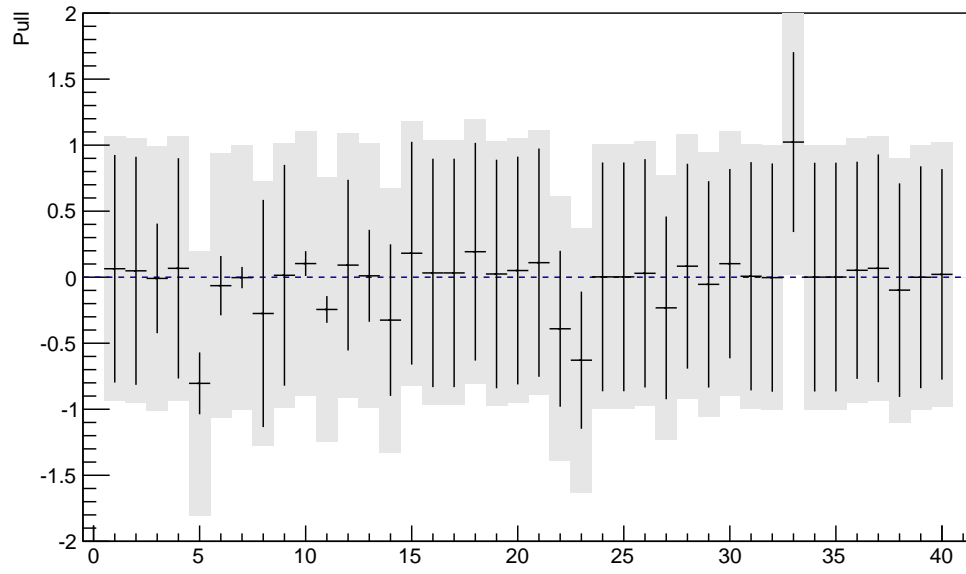
$$\sigma_{\text{norm}} = \frac{\sigma_{\text{post-fit}}}{\sigma_{\text{pre-fit}}}. \quad (8.2)$$

The σ_{norm} larger than 1 means that the nuisance is not constrained by fit.

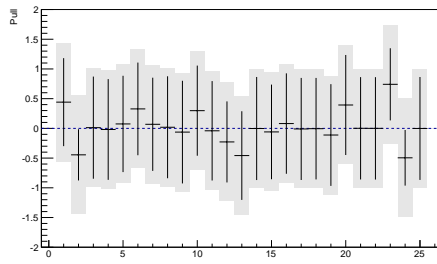
Make sure how $\sigma_{\text{post-fit}}$ is derived by the fit. can go over an example in the text book

The fig. 8.4 shows the post-fit result of nuisance parameters. The x axis is indices of nuisance parameters without any order and the y axis is for Pull and σ_{norm} . The black line shows Pull as the central value and σ_{norm} as an uncertainty bar. The grey area is drawn with Pull as central value and error bar being 1. This is to visualize the size of post-fit uncertainty with respect to the prefit uncertainty. The nuisances are divided into 5 groups; nuisances that are used (a) in all final states, (b) only in the $e\mu/\mu e$ 0jet category, (c) only in the $ee/\mu\mu$ 0jet category, (d) only in the $e\mu/\mu e$ 1jet category, and (e) only in the $ee/\mu\mu$ 1jet category.

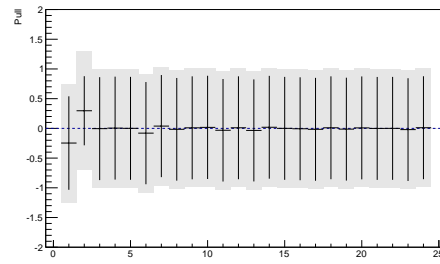
There is one nuisance parameter that has Pull greater than 1. But, it is one of the theory uncertainties on $gg \rightarrow W^+W^-$ process. Given that this process is not the dominant background process and the exact value of Pull is 1.023, this nuisance is fine. There are several nuisances that have σ_{norm} much less than 1. It is expected that σ_{norm} is less than 1, but at the same time we need to consider over-constant.



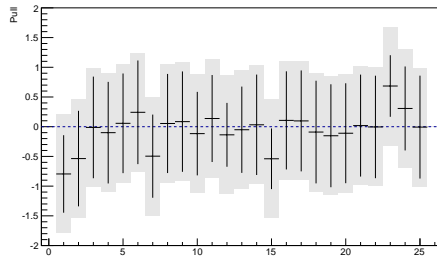
(a)



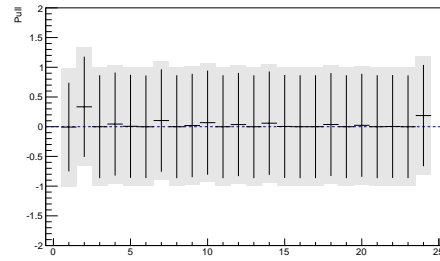
(b)



(c)



(d)



(e)

Figure 8.4: Post-fit results on the nuisance parameters.

There are 5 nuisance parameters that are constrained by more than 30 %, *i.e.* σ_{norm} is less than 0.3. They are instrumental nuisances for lepton momentum resolution, $E_{\text{T}}^{\text{miss}}$ resolution, and alternate shape nuisances for $qq \rightarrow W^+W^-$ and $t\bar{t}/tW$. The analysis is not designed to constrain the instrumental nuisances, thus some nuisances of this kind can be over-constrained allowing others nuisance not to be constrained enough. In addition removing these nuisance from the statistical interpretation does change the results at all. We discussed that the fit model for $qq \rightarrow W^+W^-$ and $t\bar{t}/tW$ were validated using dedicated control regions. So, we conclude that the over-constraint of the these nuisances is fine.

8.2.2 Correlations of nuisances

Why look at correlations? should have mentioned this way before

Fig. 8.5 shows the correlation of all 151 nuisance parameters (including signal strength). There are several bins where $|correlation|$ is larger than 0.5. These are the correlations between

Fig. 8.6 shows the correlation of selective nuisances which are normalization uncertainties of dominant processes. Here is the list of the nuisances and their meanings.

- CMS_hww_0j_WW_8TeV_SHAPE
normalization of $qq \rightarrow W^+W^-$ in $e\mu/\mu e$ 0-jet 8TeV with flat prior
- CMS_hww_0j_ttbar_8TeV
normalization of $t\bar{t}/tW$ in 0-jet 8TeV with log normal prior
- CMS_hww_1j_WW_8TeV_SHAPE
normalization of $qq \rightarrow W^+W^-$ in $e\mu/\mu e$ 1-jet 8TeV with flat prior
- CMS_hww_1j_ttbar_8TeV
normalization of $t\bar{t}/tW$ in 1-jet 8TeV with log normal prior
- CMS_hww_Wg3l
normalization of $W\gamma^*$ with log normal prior

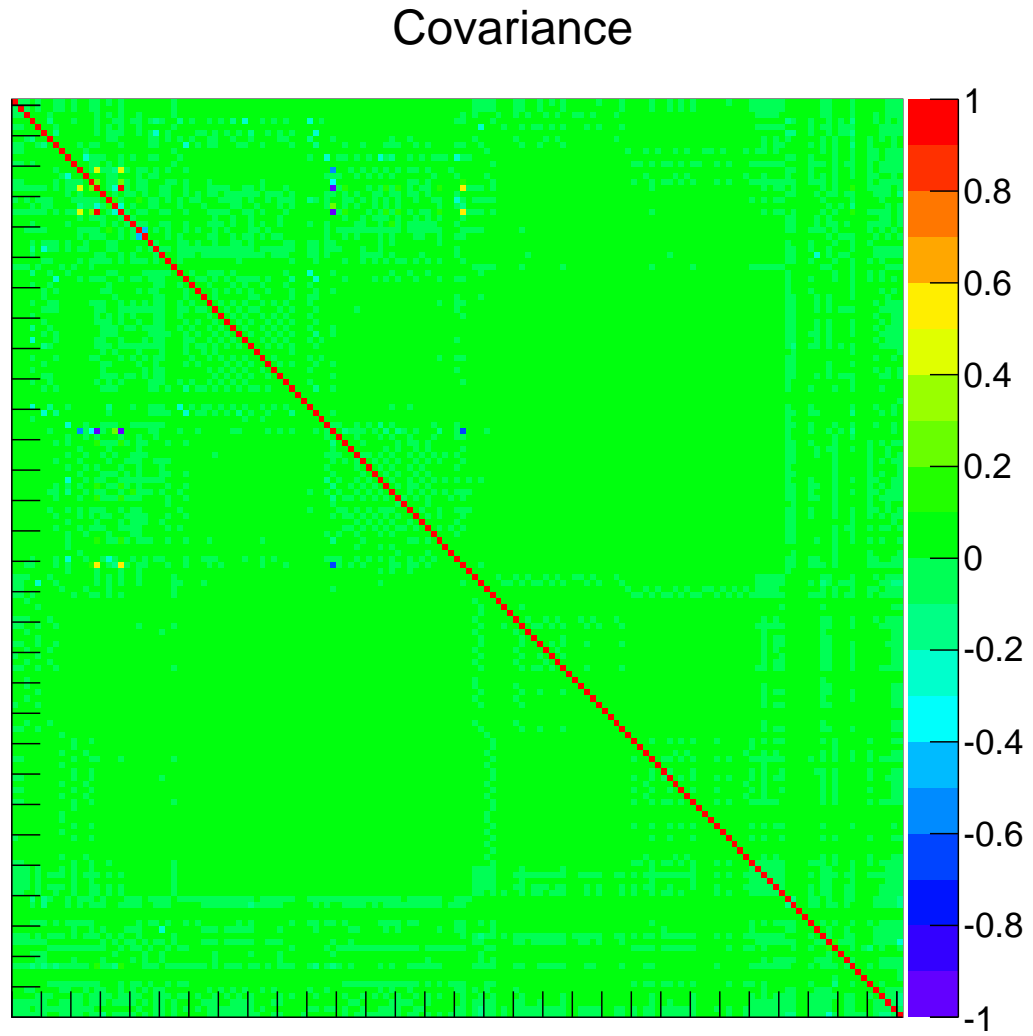


Figure 8.5: Correlation of all nuisance parameters.

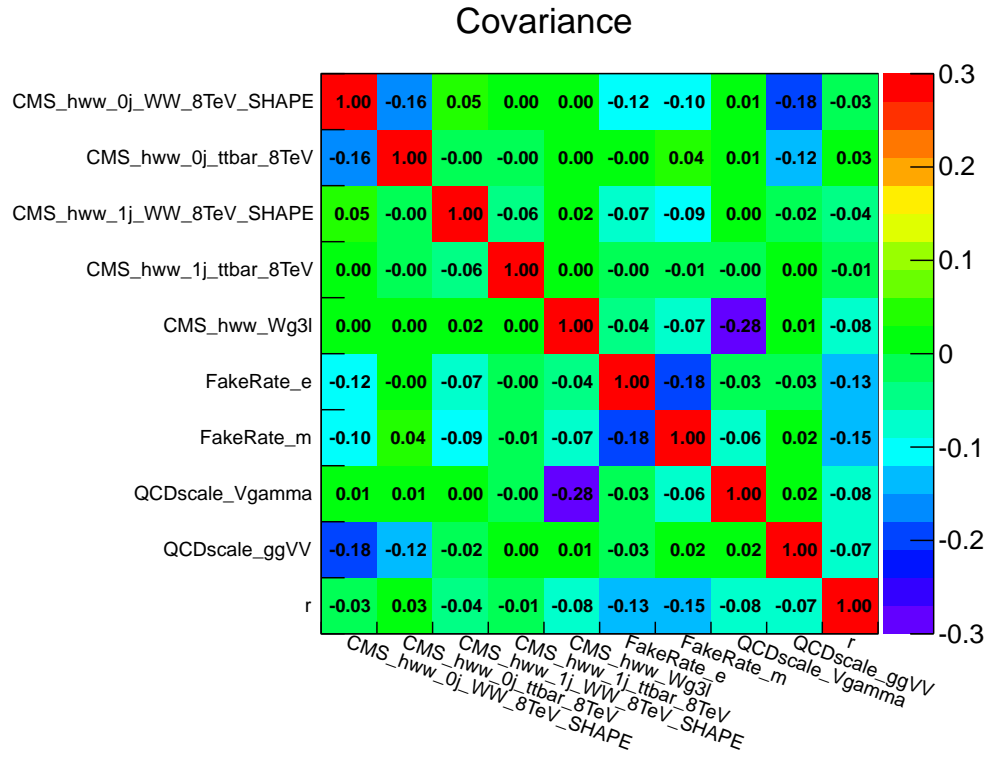


Figure 8.6: Correlation of selective nuisance parameters.

- **QCDscale_Vgamma**
normalization of $W\gamma$ with log normal prior
- **QCDscale_ggVV**
normalization of $gg \rightarrow W^+W^-$ with log normal prior
- **FakeRate_e**
normalization of $W(e\nu_e) + \text{jets}$ with log normal prior
- **FakeRate_m**
normalization of $W(\mu\nu_\mu) + \text{jets}$ with log normal prior
- **r**
signal strength with flat prior

8.2.3 Post-fit normalization

In this section we check if there is any processes of which post-fit normalization changes dramatically. A large variation which touches the boundary of the allowed uncertainty range might indicate that the fit model is not correct.

Process	N(prefit)	N(postfit)	Difference(raw)	Difference(%)
$qq \rightarrow ZH$	1.7	1.3	-0.4	-23.9
$qq \rightarrow WH$	5.7	4.5	-1.2	-20.4
$qq \rightarrow qqH$	2.9	2.2	-0.7	-23.9
$gg \rightarrow H$	228.1	169.6	-58.5	-25.6
$qq \rightarrow W^+W^-$	3981.7	3935.7	-46.0	-1.2
$gg \rightarrow W^+W^-$	211.3	292.1	80.8	38.3
WZ/ZZ	132.6	132.2	-0.4	-0.3
$t\bar{t}/tW$	499.4	422.9	-76.4	-15.3
$W(e\nu_e) + \text{jets}$	284.7	250.6	-34.1	-12.0
$W\gamma$	115.6	107.8	-7.7	-6.7
$W\gamma^*$	130.7	119.0	-11.7	-8.9
$Z \rightarrow \tau\tau$	46.0	47.2	1.3	2.7
$W(\mu\nu_\mu) + \text{jets}$	332.2	249.0	-83.2	-25.0

Table 8.4: Pre-fit and post-fit normalizations in $e\mu/\mu e$ 0jet 8TeV category

Process	N(prefit)	N(postfit)	Difference(raw)	Difference(%)
$qq \rightarrow ZH$	1.9	1.5	-0.4	-21.7
$qq \rightarrow WH$	6.9	5.4	-1.5	-21.8
$qq \rightarrow qqH$	11.1	8.5	-2.7	-24.0
$gg \rightarrow H$	88.5	68.8	-19.8	-22.3
$qq \rightarrow W^+W^-$	1203.1	1279.0	75.9	6.3
$gg \rightarrow W^+W^-$	69.0	88.4	19.4	28.1
WZ/ZZ	116.6	114.8	-1.8	-1.6
$t\bar{t}/tW$	1436.8	1348.7	-88.1	-6.1
$W(e\nu_e) + \text{jets}$	130.4	120.0	-10.4	-8.0
$W\gamma$	29.1	27.7	-1.3	-4.6
$W\gamma^*$	20.0	11.1	-8.9	-44.5
$Z \rightarrow \tau\tau$	76.8	78.9	2.2	2.9
$W(\mu\nu_\mu) + \text{jets}$	153.0	124.0	-29.0	-19.0

Table 8.5: Pre-fit and post-fit normalizations in $e\mu/\mu e$ 1jet 8TeV category

Process	N(prefit)	N(postfit)	Difference(raw)	Difference(%)
$qq \rightarrow ZH$	0.1	0.1	-0.0	-23.4
$qq \rightarrow WH$	0.5	0.4	-0.1	-23.4
$qq \rightarrow qqH$	0.5	0.4	-0.1	-23.4
$gg \rightarrow H$	55.8	41.9	-13.9	-25.0
$qq \rightarrow W^+W^-$	197.6	201.1	3.5	1.8
$gg \rightarrow W^+W^-$	9.8	12.9	3.2	32.3
WZ/ZZ	13.3	13.4	0.1	0.7
$t\bar{t}/tW$	9.3	8.8	-0.5	-5.8
$Z + \text{jets}$	92.2	100.5	8.3	9.0
$W(e\nu_e) + \text{jets}$	12.4	12.6	0.2	1.6
$W\gamma$	3.2	3.1	-0.1	-4.5
$W\gamma^*$	5.1	4.6	-0.5	-9.7
$W(\mu\nu_\mu) + \text{jets}$	16.5	17.1	0.6	3.7

Table 8.6: Pre-fit and post-fit normalizations in $ee/\mu\mu$ 0jet 8TeV category

Tables 8.4 - 8.11 show the pre-fit and post-fit normalizations of each process, and the difference in absolute yield and relative fraction in %, in each categories. In general most of the processes are stable, but $gg \rightarrow W^+W^-$ has a large change. This is driven by the nuisance, `QCDscale_ggVV`, which was pulled by 1σ .

Process	N(prefit)	N(postfit)	Difference(raw)	Difference(%)
$qq \rightarrow ZH$	0.3	0.2	-0.1	-22.9
$qq \rightarrow WH$	0.7	0.5	-0.2	-22.9
$qq \rightarrow qqH$	2.1	1.6	-0.5	-23.0
$gg \rightarrow H$	15.9	12.6	-3.3	-20.6
$qq \rightarrow W^+W^-$	37.8	39.6	1.8	4.8
$gg \rightarrow W^+W^-$	2.2	3.0	0.8	36.1
WZ/ZZ	6.5	6.6	0.1	1.7
$t\bar{t}/tW$	40.4	40.9	0.5	1.2
Z + jets	14.7	16.3	1.6	10.8
$W(e\nu_e) + \text{jets}$	2.8	2.9	0.1	2.3
$W\gamma$	2.5	2.4	-0.1	-2.1
$W\gamma^*$	0.7	0.6	-0.1	-8.4
$W(\mu\nu_\mu) + \text{jets}$	3.7	3.9	0.2	4.8

Table 8.7: Pre-fit and post-fit normalizations in $ee/\mu\mu$ 1jet 8TeV category

Process	N(prefit)	N(postfit)	Difference(raw)	Difference(%)
$qq \rightarrow qqH$	0.4	0.3	-0.1	-23.6
$gg \rightarrow H$	50.3	37.6	-12.8	-25.4
$qq \rightarrow W^+W^-$	828.8	810.5	-18.3	-2.2
$gg \rightarrow W^+W^-$	40.8	52.7	11.9	29.3
WZ/ZZ	17.7	17.8	0.1	0.6
$t\bar{t}/tW$	91.2	99.1	7.9	8.7
Z + jets	4.9	4.6	-0.4	-7.2
$W(e\nu_e) + \text{jets}$	88.3	84.4	-3.9	-4.4
$W\gamma$	19.7	18.6	-1.1	-5.5
$W\gamma^*$	36.4	35.9	-0.5	-1.5
$W(\mu\nu_\mu) + \text{jets}$	62.7	45.8	-17.0	-27.0

Table 8.8: Pre-fit and post-fit normalizations in $e\mu/\mu e$ 0jet 7TeV category

Process	N(prefit)	N(postfit)	Difference(raw)	Difference(%)
$qq \rightarrow qqH$	2.1	1.6	-0.5	-23.5
$gg \rightarrow H$	17.1	13.6	-3.5	-20.6
$qq \rightarrow W^+W^-$	246.3	273.6	27.3	11.1
$gg \rightarrow W^+W^-$	14.0	17.7	3.7	26.5
WZ/ZZ	18.1	18.1	-0.0	-0.0
$t\bar{t}/tW$	226.7	203.9	-22.8	-10.0
Z + jets	8.3	3.2	-5.1	-61.3
$W(e\nu_e) + \text{jets}$	34.4	28.5	-5.9	-17.1
$W\gamma$	3.6	3.4	-0.2	-4.3
$W\gamma^*$	4.8	5.0	0.2	3.5
$W(\mu\nu_\mu) + \text{jets}$	26.2	19.2	-7.0	-26.7

Table 8.9: Pre-fit and post-fit normalizations in $e\mu/\mu e$ 1jet 7TeV category

Process	N(prefit)	N(postfit)	Difference(raw)	Difference(%)
$qq \rightarrow qqH$	0.1	0.1	-0.0	-22.9
$gg \rightarrow H$	10.0	7.5	-2.5	-24.7
$qq \rightarrow W^+W^-$	45.0	44.5	-0.4	-1.0
$gg \rightarrow W^+W^-$	2.0	2.6	0.6	28.9
WZ/ZZ	0.9	0.9	0.0	1.3
$t\bar{t}/tW$	2.0	2.0	-0.0	-0.3
Z + jets	10.6	9.7	-0.9	-8.2
$W(e\nu_e) + \text{jets}$	2.1	2.2	0.0	0.9
$W\gamma^*$	0.7	0.7	-0.1	-9.8
$W(\mu\nu_\mu) + \text{jets}$	1.0	1.1	0.0	1.9

Table 8.10: Pre-fit and post-fit normalizations in $ee/\mu\mu$ 0jet 7TeV category

Process	N(prefit)	N(postfit)	Difference(raw)	Difference(%)
$qq \rightarrow qqH$	0.4	0.3	-0.1	-22.5
$gg \rightarrow H$	2.6	2.1	-0.5	-20.1
$qq \rightarrow W^+W^-$	9.7	9.9	0.1	1.5
$gg \rightarrow W^+W^-$	0.7	0.9	0.2	32.0
WZ/ZZ	0.7	0.7	0.0	1.9
$t\bar{t}/tW$	6.4	6.3	-0.1	-1.4
$Z + \text{jets}$	9.8	9.8	-0.0	-0.2
$W(e\nu_e) + \text{jets}$	0.7	0.7	0.0	1.6
$W\gamma^*$	0.2	0.2	-0.0	-8.8
$W(\mu\nu_\mu) + \text{jets}$	0.2	0.2	0.0	3.4

Table 8.11: Pre-fit and post-fit normalizations in $ee/\mu\mu$ 1jet 7TeV category

Chapter 9

Statistical Interpretation

9.1 Exclusion of the Standard Model Higgs Boson

The procedure of calculating observed limit is described in this section. The detailed description can be found in [9].

- **Step 1 : Construct likelihood function based on Poisson statistics**

$$\mathcal{L}(X|\mu, \theta) = \prod_i^{N_{bin}} \frac{(\mu s_i(\theta) + b_i(\theta))^{X_i}}{X_i!} e^{-\mu s_i(\theta) - b_i(\theta)} \times \prod_j^{N_{nuisance}} p(\tilde{\theta}_j|\theta_j) \quad (9.1)$$

The $X = \{X_i\}$ is a set of measurements which can be the real data from measurement or a pseudo-data generated to construct *pdfs* on a given hypothesis. N_{bin} is the number of measurements which corresponds to number of bins in the shape analysis. μ indicates the signal strength (signal strength modifier). θ is the all nuisance parameters in consideration. $s_i(\theta)$ and $b_i(\theta)$ are expected signal and background yields, respectively, in the i^{th} measurement(bin). $p(\tilde{\theta}_j|\theta_j)$ is the *pdf* for θ_j which is constructed from auxiliary measurements or some assumptions. θ_j is the measured or assumed value of θ . **need more explanation on the prior. especailly why its frequentist approach**

- **Step 2 : Construct a test static, \tilde{q}_μ**

By Neyman-Pearson lemma [ref], the ratio of two likelihoods, *i.e.* *signal+background* and *background-only*, is the most powerful discriminator. Log of the raio is taken because of a number of advantages ¹. At LHC, due to its asymptotic properties which is described in detail in Appendix A, the profiled log-likelihood ratio (LLR) is used as a test static.

$$\tilde{q}_\mu = \begin{cases} -2 \ln \frac{\mathcal{L}(X|\mu, \hat{\theta}_\mu)}{\mathcal{L}(X|\hat{\mu}, \hat{\theta})} & \text{if } 0 \leq \hat{\mu} \leq \mu \\ 0 & \text{otherwise} \end{cases} \quad (9.2)$$

¹Log converts multiplication of likelihoods into linear summation. Terms in exponent becomes a mulitplication factor.

$\hat{\theta}_\mu$ is the best-fit value of θ for a given μ . $\hat{\mu}$ and $\hat{\theta}$ are the best-fit values from global fit on data. The requirement $0 \leq \hat{\mu}$ is imposed because signal rate must be positive. $\hat{\mu} \leq \mu$ constrains for one-sided confidence level. This also means that the region, $\mu < \hat{\mu}$, is not considered more incompatible than the data observed, $\hat{\mu}$. This region is not tested for setting upper limits.

- **Step 3 : Find the observed values**

Find the observed values of the test static (\tilde{q}_μ^{obs}), and nuisance parameters ($\hat{\theta}_\mu^{obs}$ and $\hat{\theta}_0^{obs}$) that maximize the likelihoods. $\mathcal{L}(X|\mu, \hat{\theta}_\mu)$ is used to calculate \tilde{q}_μ^{obs} and $\hat{\theta}_\mu^{obs}$ for *signal + background* hypothesis with the given signal strength modifier, μ , and $\mathcal{L}(X|0, \hat{\theta}_0)$ is used to get $\hat{\theta}_0^{obs}$ for *background-only* hypothesis.

- **Step 4 : Construct *pdfs* for *signal + background* and *background-only* hypotheses**

Using the profiled nuisance parameters, $\hat{\theta}_\mu^{obs}$ and $\hat{\theta}_0^{obs}$, Monte-Carlo toys are generated to construct *pdfs* for *signal + background* and *background-only* hypotheses, $f(\hat{q}_\mu|\mu, \hat{\theta}_\mu^{obs})$ and $f(\hat{q}_\mu|0, \hat{\theta}_0^{obs})$, respectively. Since generating toys requires a large consumption of CPU power, we can take advantage of the fact that \tilde{q}_μ^{obs} follows a half χ^2 in the asymptotic limit, *i.e.* infinite statistics. This is true if $\hat{\mu} > 0$ **WHY not equal sign here?** is not applied. But, even with the requirement $\hat{\mu} > 0$, \tilde{q}_μ can be calculated analytically

$$f(\tilde{q}_\mu|\mu) = \frac{1}{2}\delta(\tilde{q}_\mu) + \begin{cases} \frac{1}{2\sqrt{2\pi}} \frac{1}{\sqrt{\tilde{q}_\mu}} e^{-\tilde{q}_\mu/2} & 0 < \tilde{q}_\mu \leq \mu^2/\sigma^2 \\ \frac{\sigma}{2\sqrt{2\pi}\mu} \exp\left[-\frac{1}{2} \frac{(\tilde{q}_\mu^2 + \mu^2/\sigma^2)^2}{(2\mu/\sigma)^2}\right] & \tilde{q}_\mu > \mu^2/\sigma^2 \end{cases} \quad (9.3)$$

where $\delta(\tilde{q}_\mu)$ is Dirac delta function. $\sigma^2 = \frac{\mu^2}{q_{\mu,A}}$ is the uncertainty on the test statistics evaluated using Asimov data set. Asimov dataset is a representative dataset made with expected background and nuisance parameters. This is the dataset that corresponds to the infinite statistics. In this analysis expected sensitivity(exclusion and significance) is calculated in the asymptotic limit. Similarly, the *pdf* for the *background-only* hypothesis, $f(\tilde{q}_\mu|0)$, can be obtained using the same technique. The two *pdfs* are used to construct a measure for hypothesis test.

• **Step 5 : Calculated statistical significance of observation**

For the measurement X, the test static, \tilde{q}_μ^{obs} , can be used to test significance of the observation. At LEP, modified frequentist method (CL_s) was developed in order to mitigate the problem of having downward fluctuation in data where small signal strength. LHC uses the same technique. CL_s is defined by two p-values, p_μ and $1 - p_b$. p_μ is the p-value with *signal + background* hypothesis and defined by

$$p_\mu = P(\tilde{q}_\mu \geq \tilde{q}_\mu^{obs} | \text{signal} + \text{background}) \quad (9.4)$$

$$= \int_{\tilde{q}_\mu^{obs}}^{\infty} f(\tilde{q}_\mu | \mu) d\tilde{q}_\mu. \quad (9.5)$$

Larger value of p_μ represents a high chance that observation is compatible with the hypothesed signal strength, μ . $1 - p_b$ is the p-value with *background-only* hypothesis and defined by

$$1 - p_b = P(\tilde{q}_\mu \geq \tilde{q}_\mu^{obs} | \text{background} - \text{only}) \quad (9.6)$$

$$= \int_{\tilde{q}_\mu^{obs}}^{\infty} f(\tilde{q}_\mu | 0) d\tilde{q}_\mu. \quad (9.7)$$

Larger value of $1 - p_0$ represents a high chance that observation is compatible with the null hypothesis, $\mu = 0$. Thus, p_b is low if data is *signal + background*-like. CL_s is defined as a ratio of the two p-values

$$CL_s(\mu) = \frac{p_\mu}{1 - p_b}. \quad (9.8)$$

Upper limit on μ at $\alpha\%$ Confidence level is the value of μ which gives $CL_s = 1 - \alpha\%$. Writing for μ ,

$$\mu^{\alpha\%} = CL_s^{-1}(1 - \alpha\%). \quad (9.9)$$

In this case, the *signal+background* hypothesis with $\mu > \mu^{\alpha\%}$ is incompatible with data and said to be excluded at $\alpha\%$ CL_s confidence level. It is useful to know how expected $\mu^{\alpha\%}$ varies by fluctuation in data because even though the true μ (call it μ') is correct, data we actually observe can have different value by statistical fluctuation. The median expected limits and its uncertainty bands ($\pm N\sigma$) assuming *background-only* hypothesis ($\mu' = 0$) are given by

$$\mu_{\pm N\sigma}^{up} = \sigma (\Phi^{-1}(1 - \alpha) \pm N). \quad (9.10)$$

where Φ is a cumulative distribution of standard normal distribution. Why is equation different in [9]? Where is $\Phi(N)$ from? Real results have asym bands. How can explain this?

9.2 Discovery of a New Boson

In order to claim a discovery of a new particle, we test the compatibility of *background-only* hypothesis against data. Large deviation in p-value indicates that the observed data is not compatible with *background-only* hypothesis, thus something "new" needs to be taken into account. This test can be performed by throwing many "pseudo-data" assuming *background-only* hypothesis and construct *pdf* for the choice of test statistic. The choice of test statistic is the following.

$$q_0 = \begin{cases} -2 \ln \frac{\mathcal{L}(X|0, \hat{\theta}_0)}{\mathcal{L}(X|\mu, \hat{\theta}_\mu)} & \text{with } \hat{\mu} \geq 0 \\ 0 & \text{with } \hat{\mu} < 0 \end{cases} \quad (9.11)$$

We don't consider downward fluctuation in data ($\hat{\mu} < 0$) as a incompatibility with data as upward fluctuation. Downward fluctuation is more likely due to systematic uncertainties such as over-estimation of backgrounds. So, in case of $\hat{\mu} < 0$ the test statistic is set 0. Given the test statistic, construct *pdf*, $f(q_0|0, \hat{\theta}_0)$, with many pseudo-datasets generated assuming *background-only* hypothesis. The p-value for the observation, q_0^{obs} , is given by

$$p_0 = P(q_0 \geq q_0^{obs} | \text{background} - \text{only}) \quad (9.12)$$

$$= \int_{q_0^{obs}}^{\infty} f(q_0|0, \hat{\theta}_0) dq_0. \quad (9.13)$$

The calculated p-value can be converted into an one-sided(Why one-sided?) significance Z by finding Z that satisfies

$$p - \text{value} = \int_Z^{\infty} \frac{1}{\sqrt{2\pi}} e^{-\frac{x^2}{2}} dx. \quad (9.14)$$

In the asymptotic limit, the *pdf* is given by

$$f(q_0|0, \hat{\theta}_0) = \frac{1}{2} \delta(q_0) + \frac{1}{2\sqrt{2\pi}\sqrt{q_0}} e^{-\frac{q_0}{2}}. \quad (9.15)$$

In this case p-value can be obtained by

$$p_0 = 1 - \Phi(\sqrt{q_0}). \quad (9.16)$$

Using this equation, the significance is given by

$$Z_0 = \Phi^{-1}(1 - p_0) = \sqrt{q_0}. \quad (9.17)$$

The sensitivity to discovery of a process is often measured by expected significance. It is the p-value obtained by a pseudo-dataset assuming $\mu = 1$.

9.3 Hypothesis Separation

Once a particle is observed, it is important to test its properties such as mass, spin, parity, *etc.* It is shown that the full leptonic WW analysis is sensitive to distinguish between SM model hypothesis and a spin-2 resonance, which couples to the dibosons through minimal couplings [10].

We perform MLL fit to each hypothesis to extract the signal strength and background contributions. The same likelihood function as SM Higgs search is used. For a given dataset, MLL fits for both hypotheses are performed. In the likelihood calculation, the signal strength is allowed to float as SM Higgs search. The signal strength and nuisance parameters of the two hypotheses are treated independently. The difference in the best-fit likelihoods

$$q = -2 \ln \frac{\mathcal{L}_{2^+}}{\mathcal{L}_{0^+}} = -2 \ln \frac{\mathcal{L}(X|\hat{\mu}_{2^+}, \hat{\theta}_{2^+})}{\mathcal{L}(X|\hat{\mu}_{0^+}, \hat{\theta}_{0^+})} \quad (9.18)$$

is used to quantify the consistency of data to the two hypothesis.

Chapter 10

Study on Spin-Parity of the New Boson

Appendix A

Some Details on Statistical Procedure

This chapter describes some of the statistical procedures in detail.

A.1 Asimov data set

When [11]

A.2 Asymtotic behavior of profiled LLR

Bibliography

- [1] V. Barger, K. Cheung, A. Djouadi, B. A. Kniehl, and P. M. Zerwas. Higgs bosons: Intermediate mass range at e^+e^- colliders. *Phys. Rev. D*, 49:79–90, Jan 1994.
- [2] Abdelhak Djouadi. The anatomy of electroweak symmetry breaking: Tome i: The higgs boson in the standard model. *Physics Reports*, 457(14):1 – 216, 2008.
- [3] Christopher F. Kolda and Hitoshi Murayama. The Higgs mass and new physics scales in the minimal standard model. *JHEP*, 0007:035, 2000.
- [4] The ALEPH, DELPHI, L3, OPAL Collaborations, the LEP Electroweak Working Group. Electroweak Measurements in Electron-Positron Collisions at W-Boson-Pair Energies at LEP. 2013.
- [5] J. Beringer et al. Review of Particle Physics (RPP). *Phys.Rev.*, D86:010001, 2012.
- [6] CMS Collaboration. Combined results of searches for the standard model higgs boson in pp collisions at. *Physics Letters B*, 710(1):26 – 48, 2012.
- [7] ATLAS Collaboration. Combined search for the standard model higgs boson using up to 4.9 fb^{-1} of pp collision data at with the atlas detector at the lhc. *Physics Letters B*, 710(1):49 – 66, 2012.
- [8] CMS Collaboration. Search for the standard model higgs boson decaying to in the fully leptonic final state in pp collisions at. *Physics Letters B*, 710(1):91 – 113, 2012.
- [9] CMS Collaborations The ATLAS and the LHC Higgs Combination Group. *Procedure for the LHC Higgs boson search combination in summer 2011. ATL-PHYS-PUB-2011-11, CMS-NOTE-2011-005*, 2011.
- [10] A. V. Gritsan et al S. Bolognesi, Y. Gao. *On the spin and parity of a single-produced resonance at the LHC*. arXiv:1208.4018.

- [11] E. Gross G. Cowan, K. Cranmer and O. Vitells. *Asymptotic formulae for likelihood-based tests of new physics. The European Physical Journal C*, **71**:1–19, 2011.